Received November 2001
Revised May 2002
Accepted May 2002

Non-linear explicit dynamic analysis of shells using the BST rotation-free triangle

E. Oñate
International Centre for Numerical Methods in Engineering, Universidad Politécnica de Cataluña, Barcelona, Spain

P. Cendoya
Universidad de Concepción, Concepción, Chile

J. Miquel
International Centre for Numerical Methods in Engineering, Universidad Politécnica de Cataluña, Barcelona, Spain

Keywords *Non-linear, Dynamic analysis, Shells, Boundary conditions*

Abstract *The paper describes the application of the simple rotation-free basic shell triangle (BST) to the non-linear analysis of shell structures using an explicit dynamic formulation. The derivation of the BST element involving translational degrees of freedom only using a combined finite element–finite volume formulation is briefly presented. Details of the treatment of geometrical and material non linearities for the dynamic solution using an updated Lagrangian description and an hypoelastic constitutive law are given. The efficiency of the BST element for the non linear transient analysis of shells using an explicit dynamic integration scheme is shown in a number of examples of application including problems with frictional contact situations.*

1. Introduction

The solution of large scale shell problems such as those occurring in many practical engineering situations requires the use of simple and efficient shell elements. Typical examples are the analysis of shell roofs, sheet stamping processes, vehicle dynamics and crash-worthiness situations. The natural difficulties of these problems, typically involving time changing frictional contact conditions, is increased by the need of discretizing complex geometrical shapes. Here the use of shell triangles and non-structured meshes becomes a

The authors are grateful to Drs F. Zarate, J. Rojek and F. Flores for many useful discussions. Thanks are also given to Quantech ATZ SA for providing access to the commercial sheet stamping code STAMPACK where the BST element is implemented (STAMPACK, 2002). This research has been partially supported by the Ministerio de Ciencia y Tecnologa (Spain) through project 2FD1997-0336-C03-01 (TAP).

Engineering Computations,
Vol. 19 No. 6, 2002, pp. 662-706.

DOI 10.1108/02644400210439119

critical necessity. Unfortunately, despite recent advances in the field (Zienkiewicz and Taylor, 2000; Stolarski *et al.*, 1995; Oñate, 1999; Ghali and Bathe, 1970; ECCOMAS, 2000) there are not so many simple shell triangles which are capable of accurately modeling the deformation of a shell structure under arbitrary loading conditions.

A promising line to derive simple shell triangles is to use the nodal displacements as the only unknown for describing the shell kinematics. This idea goes back to the original attempts to solve thin plate bending problems using finite difference schemes with the deflection as the only nodal variable (Ghali and Bathe, 1970; Bushnell and Almroth, 1971; Timoshenko, 1979; Uguraz, 1981).

In recent years some authors have derived a number of thin plate and shell triangular elements free of rotational degrees of freedom based on Kirchhoff's theory (Nay and Utku, 1972; Hampshire *et al.*, 1992; Phaal and Calladine, 1992a, b; Yang *et al.*, 1993; Brunet and Sabourin, 1994; Rio *et al.*, 1994; Cirak *et al.*, 2000). In essence, all methods attempt to express the curvatures field over an element in terms of the displacements of a collection of nodes belonging to a patch of adjacent elements. Oñate and Cervera (1993) proposed a general procedure of this kind combining finite element and finite volume concepts for deriving thin plate triangles and quadrilaterals with the deflection as the only nodal variable and presented a simple and competitive rotation-free three d.o.f. triangular element termed basic plate triangle (BPT). These ideas were extended and formalized by Oñate and Zárate (2000) to derive a number of rotation-free thin plate and shell triangles. The basic ingredients of the method are a mixed Hu–Washizu formulation, a standard discretization into three-node triangles, a linear finite element interpolation of the displacement field within each triangle and a finite volume type approach for computing the curvature and bending moment fields within appropriate non-overlapping control domains. The so called "cell-centered" and "cell-vertex" triangular domains were explored, yielding different families of rotation-free plate and shell triangles. Both the BPT plate element and its extension to shell analysis (termed basic shell triangle (BST) element) can be derived from the cell-centered formulation. The cell-vertex approach yields a different family of rotation-free plate and shell triangles. Details of the derivation of both triangular element families are reported by Oñate and Zárate (2000). An extension of the BST element to large strain plasticity problems has been reported by Flores and Oñate (2001).

In this paper the BST is extended for non-linear dynamic analysis of shells. The "control domain" corresponding to this element is an individual triangle. The constant curvatures field over the triangle is computed in terms of the displacements of the six nodes belonging to the four elements patch formed by the central triangle and the three adjacent triangles.

The layout of the paper is as follows. In Section 1.1, the basic formulation of the BST element is briefly described. Details of the extension to non-linear

dynamic analysis using an updated Lagrangian description and an hypoelastic constitutive model is then presented. Next, the explicit dynamic algorithm for non-linear dynamic analysis of shell problems involving frictional contact condition is detailed. The accuracy of the rotation-free BST element for non linear structural dynamic analysis is shown in the solution of a number of non linear shell problems including the analysis of three sheet stamping processes.

1.1 Basic theory

Let us consider the planar shell domain of Figure 1. We will assume Kirchhoff's orthogonality conditions to hold, i.e.

$$\theta_{x'} = \frac{\partial w'}{\partial x'} \quad \text{and} \quad \theta_{y'} = \frac{\partial w'}{\partial y'} \tag{1}$$

where w' is the displacement in the normal direction. As usual x' and y' denote the local in-plane directions (Figure 1).

The bending moment–curvature and the axial force–elongation relationships are expressed in the usual form (in local axes) as

$$\mathbf{m}' = \mathbf{D}_{\mathrm{b}}\boldsymbol{\kappa}' \qquad \mathbf{n}' = \mathbf{D}_{\mathrm{m}}\boldsymbol{\lambda}' \tag{2}$$

with

$$\begin{gathered}
\mathbf{m}' = [m_{x'}, m_{y'}, m_{x'y'}]^{\mathrm{T}} \qquad \mathbf{n}' = [n_{x'}, n_{y'}, n_{x'y'}]^{\mathrm{T}} \\
\boldsymbol{\kappa}' = [\kappa_{x'}, \kappa_{y'}, \kappa_{x'y'}]^{\mathrm{T}} = \mathbf{L}_{\mathrm{b}} w' \quad \mathbf{L}_{\mathrm{b}} = \left[-\frac{\partial^2}{\partial x'^2}, -\frac{\partial^2}{\partial y'^2}, -\frac{2\partial^2}{\partial x' \partial y'} \right]^{\mathrm{T}} \\
\boldsymbol{\lambda}' = [\lambda_{x'}, \lambda_{y'}, \lambda_{x'y'}]^{\mathrm{T}} = \mathbf{L}_{\mathrm{m}} \mathbf{u}' \quad \mathbf{u}' = \begin{Bmatrix} u' \\ v' \end{Bmatrix} \quad \mathbf{L}_{\mathrm{m}} = \begin{bmatrix} \frac{\partial}{\partial x'} & 0 \\ 0 & \frac{\partial}{\partial y'} \\ \frac{\partial}{\partial y'} & \frac{\partial}{\partial x'} \end{bmatrix}
\end{gathered} \tag{3}$$

where u' and v' are the in-plane displacements (Figure 1). For an isotropic homogeneous material

$$\mathbf{D}_{\mathrm{b}} = \frac{Eh^3}{12(1-\nu^2)} \begin{bmatrix} 1 & \nu & 0 \\ \nu & 1 & 0 \\ 0 & 0 & \frac{1-\nu}{2} \end{bmatrix} \qquad \mathbf{D}_{\mathrm{m}} = \frac{Eh}{(1-\nu^2)} \begin{bmatrix} 1 & \nu & 0 \\ \nu & 1 & 0 \\ 0 & 0 & \frac{1-\nu}{2} \end{bmatrix} \tag{4}$$

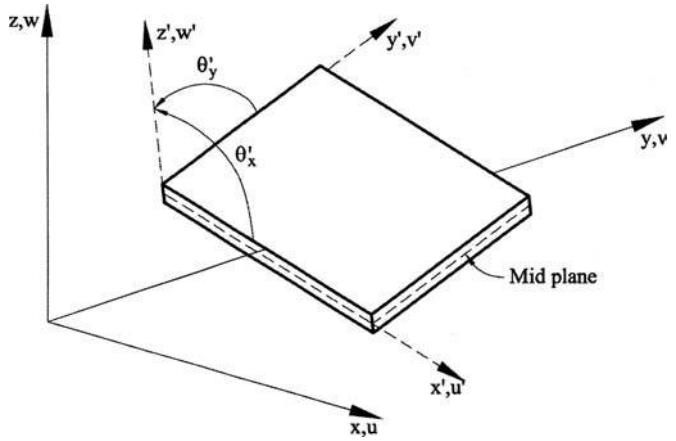

Figure 1.
Planar shell element. Definition of global and local axes, displacements and rotations

where E and ν are the Young's modulus and the Poisson's ratio, respectively, and h is the shell thickness.

The set of governing equations is expressed in integral form starting from the modified Hu-Washizu functional (Zienkiewicz and Taylor, 2000)

$$\Pi = \frac{1}{2}\iint_A \boldsymbol{\kappa}'^{\mathrm{T}}\mathbf{D}_{\mathrm{b}}\boldsymbol{\kappa}'\,\mathrm{d}A + \frac{1}{2}\iint_A [\mathbf{L}_{\mathrm{m}}\mathbf{u}']^{\mathrm{T}}\mathbf{D}_{\mathrm{m}}[\mathbf{L}_{\mathrm{m}}\mathbf{u}']\,\mathrm{d}A - \iint_A [\mathbf{L}_{\mathrm{b}}w' - \boldsymbol{\kappa}']^{\mathrm{T}}\mathbf{m}'\,\mathrm{d}A - \iint_A \mathbf{u}^{\mathrm{T}}\mathbf{q}\,\mathrm{d}A \tag{5}$$

where $\mathbf{q} = [q_x, q_y, q_z]^{\mathrm{T}}$ is the distributed load vector (in global axes), $\mathbf{u} = [u, v, w]^{\mathrm{T}}$ is the global displacement vector and A is the area of the shell surface.

Variations of Π with respect to $\boldsymbol{\kappa}'$, $\mathbf{m}'$ and the displacements lead to the following integral equations.

1.1.1 Bending moment–curvature equations

$$\iint_A \delta\boldsymbol{\kappa}'^{\mathrm{T}}[\mathbf{D}_{\mathrm{b}}\boldsymbol{\kappa}' - \mathbf{m}']\,\mathrm{d}A = 0 \tag{6}$$

1.1.2 Curvature–defection equation

$$\iint_A \delta\mathbf{m}'^{\mathrm{T}}[\mathbf{L}_{\mathrm{b}}w' - \boldsymbol{\kappa}']\,\mathrm{d}A = 0 \tag{7}$$

1.1.3 Equilibrium equation

$$\iint_A [\mathbf{L}5_b \delta w']^T \mathbf{m}' \, dA + \iint_A [\mathbf{L}_m \delta \mathbf{u}']^T \mathbf{D}_m [\mathbf{L}_m \mathbf{u}'] \, dA - \iint_A \delta \mathbf{u}^T \mathbf{q} \, dA = 0 \quad (8)$$

Equations (6)–(8) are the basis for the discretization of the shell to be presented next

1.2 Finite element/finite volume discretization

Let us consider an arbitrary discretization of the shell surface into standard three-node triangles. The curvatures and the bending moments are described by constant fields within appropriate *non-overlapping control domains* (also termed "control volumes" in the finite volume (FV) literature (Zienkiewicz and Oñate, 1991; Oñate *et al.*, 1994; Idelsohn and Oñate, 1994)) covering the whole shell surface as

$$\mathbf{m}' = \mathbf{I}_3 \mathbf{m}'_p \qquad \delta \mathbf{m}' = \mathbf{I}_3 \delta \mathbf{m}'_p \quad (9a)$$

$$\boldsymbol{\kappa}' = \mathbf{I}_3 \boldsymbol{\kappa}'_p \qquad \delta \boldsymbol{\kappa}' = \mathbf{I}_3 \delta \boldsymbol{\kappa}'_p \quad (9b)$$

where $\mathbf{I}_3$ is the 3×3 unit matrix and $(\cdot)_p$ denotes constant values for the pth control domain.

The modality of control domain considered here is that formed by a single triangular element (Figure 2). This option is termed in the FV literature "cell-centered" scheme. Note that in the cell-centered scheme each control domain coincides with a standard three-node finite element triangle. Alternatively, a cell-vertex scheme can be chosen as described by Oñate and Zárate (2000). This option will not be considered here.

It is also useful to define the term "patch of elements" associated to a control domain. In the cell-centered scheme (Figure 2), this patch is always formed by four elements (except for the elements sharing a boundary segment).

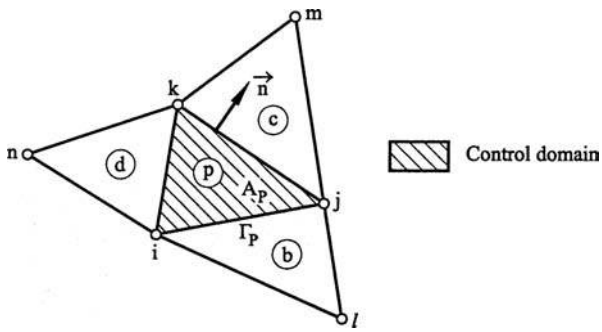

Figure 2.
Cell-centered finite volume. Control domain and patch of four three-node triangles

The name "cell-centered" indicates that the chosen variables (i.e. the curvatures and the bending moments) are "sampled" at the center of the cells discretizing the analysis domain (i.e. the three-node triangles).

The constant curvature and bending moment fields within each control domain are expressed next in terms of the nodal deflections associated to the corresponding patch of triangular elements.

The area integrals in equations (6)–(8) can be written as the sum of the contributions over the different control domains taking into account equation (9) as

1.2.1 Constitutive equation

$$\sum_{p} \iint_{A_p} \delta\boldsymbol{\kappa}_p'^{\mathrm{T}} [\mathbf{D}_{\mathrm{b}} \boldsymbol{\kappa}_p' - \mathbf{m}_p'] \, \mathrm{d}A = 0 \tag{10}$$

where A_p is the area of the pth control domain.. Recalling that the virtual curvatures are arbitrary, gives

$$\boxed{\mathbf{m}_p' = \mathbf{D}_{\mathrm{b}_p} \boldsymbol{\kappa}_p'} \tag{11}$$

$$\mathbf{D}_{\mathrm{b}_p} = \frac{1}{A_p} \iint_{A_p} \mathbf{D}_{\mathrm{b}} \, \mathrm{d}A \tag{12}$$

where $\mathbf{D}_{\mathrm{b}_p}$ is the average bending constitutive matrix over a control domain. Equation (11) defines the constant bending moment field over the control domain in terms of the corresponding constant curvatures.

1.2.2 Curvature–deflection equation

$$\sum_{p} \iint_{A_p} \delta\mathbf{m}_p'^{\mathrm{T}} [\mathbf{L}5_{\mathrm{b}} w' - \boldsymbol{\kappa}_p'] \, \mathrm{d}A = 0 \tag{13}$$

Taking into account that the virtual bending moments are arbitrary, gives:

$$\boldsymbol{\kappa}_p' = \frac{1}{A_p} \iint_{A_p} \mathbf{L}_{\mathrm{b}} w' \, \mathrm{d}A \tag{14}$$

The integration by parts of the r.h.s. of equation (14) leads to

$$\boxed{\boldsymbol{\kappa}_p' = \frac{1}{A_p} \int_{\Gamma_p} \mathbf{T} \boldsymbol{\nabla}' w' \, \mathrm{d}\Gamma} \tag{15}$$

where

$$\boldsymbol{\nabla}' = \begin{Bmatrix} \dfrac{\partial}{\partial x'} \\ \dfrac{\partial}{\partial y'} \end{Bmatrix}$$

and $\mathbf{T}$ is a matrix depending on the outward unit normal to the boundary Γ_p surounding the control domain. For flat control domains

$$\mathbf{T} = \begin{bmatrix} -n_x & 0 & -n_y \\ 0 & -n_y & -n_x \end{bmatrix}^{\mathrm{T}} \tag{16}$$

and $\mathbf{n} = [n_x, n_y]^{\mathrm{T}}$ is the outward unit normal to the boundary Γ_p surrounding the control domain (Figure 2).

Equation (15) defines the curvatures for each control volume in terms of the deflection gradients along its boundaries. The transformation of the area integral of equation (14) into the line integral of equation (15) is typical of FV methods (Zienkiewicz and Oñate, 1991; Oñate *et al.*, 1994; Idelsohn and Oñate, 1994).

The computation of the line integral in equation (15) poses a difficulty for cases where the deflection gradient is discontinuous at the control volume boundaries and some smoothing procedure is then required. This issue is discussed in more detail in a later section.

1.2.3 Equilibrium equation. Equation (8) can be expressed as:

$$\sum_p \iint_{A_p} [\mathbf{L}\delta w']^{\mathrm{T}} \mathbf{m}'_p \, \mathrm{d}A + \iint_A [\mathbf{L}_{\mathrm{m}} \delta \mathbf{u}']^{\mathrm{T}} \mathbf{D}_{\mathrm{m}} [\mathbf{L}_{\mathrm{m}} \mathbf{u}'] \, \mathrm{d}A - \iint_A \delta w' \mathbf{q} \, \mathrm{d}A = 0 \tag{17}$$

Integrating by parts the first integral in equation (17) and recalling that the bending moments are constant within each control domain, gives:

$$\sum_p \left(\int_{\Gamma_p} [\mathbf{T}\boldsymbol{\nabla}' \delta w']^{\mathrm{T}} \, \mathrm{d}\Gamma \right) \mathbf{m}'_p + \iint_A [\mathbf{L}_{\mathrm{m}} \delta \mathbf{u}']^{\mathrm{T}} \mathbf{D}_{\mathrm{m}} [\mathbf{L}_{\mathrm{m}} \mathbf{u}'] \, \mathrm{d}A - \iint_A \delta w' \mathbf{q} \, \mathrm{d}A = 0 \tag{18}$$

Substituting equations (11) and (15) into (18) finally gives:

$$\sum_{p}\left(\int_{\Gamma_p}[\mathbf{T}\boldsymbol{\nabla}'\delta w']^{\mathrm{T}}\,\mathrm{d}\Gamma\right)\frac{1}{A_p}\mathbf{D}_{\mathrm{b}_p}\int_{\Gamma_p}\mathbf{T}\boldsymbol{\nabla}' w'\,\mathrm{d}\Gamma + \iint_A[\mathbf{L}_{\mathrm{m}}\delta\mathbf{u}']^{\mathrm{T}}\mathbf{D}_{\mathrm{m}}[\mathbf{L}_{\mathrm{m}}\mathbf{u}']\,\mathrm{d}A - \iint_A \delta\mathbf{u}^{\mathrm{T}}\mathbf{q}\,\mathrm{d}A = 0 \tag{19}$$

The next step is to discretize the displacement field within each finite element (FE). The simplest option is to interpolate linearly the deflection field within each triangle in terms of the nodal values in the standard manner (Zienkiewicz and Taylor, 2000) as

$$\begin{Bmatrix} u' \\ v' \\ w' \end{Bmatrix} = \sum_{i=1}^{3} N_i \begin{Bmatrix} u'_i \\ v'_i \\ w'_i \end{Bmatrix} \tag{20}$$

where N_i are the linear shape functions of the three-node triangle and $(\cdot)'_i$ denotes nodal values of the local displacements.

Substituting equation (20) into (19) leads, after the usual transformation to global displacements, to the standard system of stiffness equations for the shell relating global nodal forces with global nodal displacements.

Derivation of the BST rotation-free shell triangle based on the combination of a cell-centered scheme and a linear FE interpolation is briefly presented next. For more details, refer Oñate and Zárate (2000)

2. Formulation of the BST element

Figure 3 shows the patch of four shell triangles typical for the BST element. We will focus in the derivation of the stiffness equations for the BST element which is the central triangle in the patch. Also in Figure 3 the local and global node numbering scheme chosen is shown. A clear definition of local and global node numbers is essential for the derivation of the element stiffness matrix as shown next.

Figure 4 shows the local element axes $x'y'z'$, where x' is parallel to side i–j and in the direction of increasing local node numbers, z' is a direction orthogonal to the element defining the unit normal vector $\mathbf{n}$ and y' is obtained by cross product of vectors along z' and x'. A side coordinate system is also defined (see Figures 4 and 5) including side unit vectors $\mathbf{s}$, $\mathbf{t}$ and $\mathbf{n}$. Vector $\mathbf{s}$ is aligned along the side following the directions of increasing global node numbers, $\mathbf{n}$ is the normal vector parallel to the z' local axis and $\mathbf{t} = \mathbf{n} \wedge \mathbf{s}$.

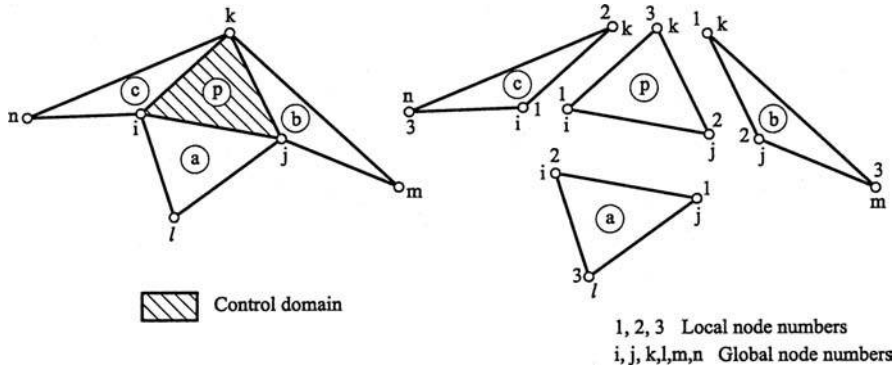

Figure 3.
BST element. Control domain and four elements patch

For simplicity let us express the local rotations $\theta_{x'}, \theta_{y'}$ along each side in terms of the tangential and normal side rotations θ_s and θ_n. The sign of the rotations follows the criterion of Figures 4 and 5.

The transformation relating local and side rotations is written as

$$\theta'^{(p)} = \begin{Bmatrix} \theta_{x'} \\ \theta_{y'} \end{Bmatrix}^{(p)} = \begin{bmatrix} c_{ij} & -s_{ij} \\ s_{ij} & c_{ij} \end{bmatrix}^{(p)} \begin{Bmatrix} \theta_{s_{ij}} \\ \theta_{n_{ij}} \end{Bmatrix}^{(p)} = \hat{\mathbf{T}}_{ij} \hat{\theta}'_{ij} \tag{21}$$

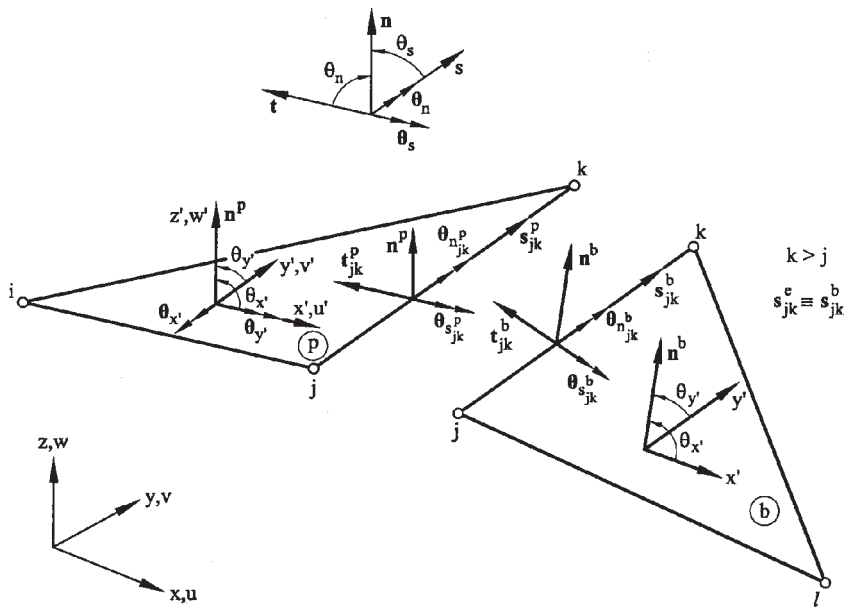

Figure 4.
BST element. Definition of global, local and side coordinate systems

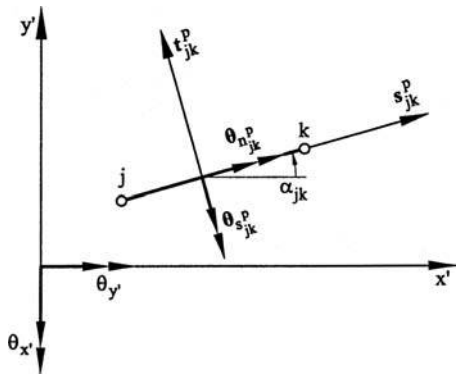

Figure 5.
BST element. Transformation from side rotations to local rotations

where $\theta_{s_{ij}}$ and $\theta_{n_{ij}}$ are the tangential and normal rotations along the side ij of element p, $\theta_{x'} = \partial w'/\partial x'$, $\theta_{y'} = \partial w'/\partial y'$ and $c_{ij}^{(p)}$, $s_{ij}^{(p)}$ are the components of the side vector $\mathbf{s}_{ij}^{(p)}$, i.e. $\mathbf{s}_{ij}^{(p)} = [c_{ij}^{(p)}, s_{ij}^{(p)}]^{\mathrm{T}}$.

The c onstant local curvatures field over the triangle ijk is defined in terms of the deflection gradient along the element sides by equation (15).

The next step is to define a linear interpolation of the local displacements over the triangle. This obviously leads to a discontinuity of the deflection gradients across adjacent elements and a smoothing procedure is required as described next.

Recalling that $\theta' = [\theta_{x'}, \theta_{y'}]^{\mathrm{T}} = \boldsymbol{\nabla}' w'$ and substituting equation (21) into (25), the curvature over the pth triangle can be written as

$$\boldsymbol{\kappa}'_p = \frac{1}{A^{(p)}}[\mathbf{T}_{ij}^{(p)}\hat{\mathbf{T}}_{ij}^{(p)}\hat{\theta}'_{ij}l_{ij} + \mathbf{T}_{jk}^{(p)}\hat{\mathbf{T}}_{jk}^{(p)}\hat{\theta}'_{jk}l_{jk} + \mathbf{T}_{ki}^{(p)}\hat{\mathbf{T}}_{ki}^{(p)}\hat{\theta}'_{ki}l_{ki}] \tag{22}$$

In the derivation of equation (22) it has been assumed that the local rotations are constant over each element side. This is a consequence of the linear interpolation chosen for the displacement field.

The tangential side rotations can be directly expressed in terms of the local deflections along the sides. For instance, for side jk

$$\theta_{s_{jk}}^{(p)} = \frac{w'^{(p)}_k - w'^{(p)}_j}{l_{jk}} \quad \text{for } k > j \tag{23}$$

where l_{jk} is the length of side jk.

Equation (23) introduces an approximation as the tangential rotation vectors of adjacent elements sharing a side that are not parallel. Therefore the tangential rotation are discontinuous along element sides, i.e. (see Figure 4)

$$\theta_{s_{jk}}^{(p)} = \frac{w'^{(p)}_k - w'^{(p)}_j}{l_{jk}} \neq \frac{w'^{(b)}_k - w'^{(b)}_j}{l_{jk}} = \theta_{s_{jk}}^{(b)} \tag{24}$$

The authors have found that this error has little relevance in practice. Note that the error diminishes for smooth shells as the mesh is refined. Thus, for quasi-coplanar sides $w'^{(p)}_k \simeq w'^{(b)}_k$, $w'^{(p)}_j \simeq w'^{(b)}_j$ and, consequently, $\theta_{s_{jk}}^{(p)} \simeq \theta_{s_{jk}}^{(b)}$ (Oñate and Zárate, 2000).

The normal rotation vector has the same direction for the two elements sharing a side (Figure 4). A *continuous* value of the normal rotation along the side can be enforced by defining an *average* normal side rotation as:

$$\theta_{n_{jk}}^{(p)} = \tfrac{1}{2}(\theta_{n_{jk}}^{(p)} + \theta_{n_{jk}}^{(b)}) \tag{25}$$

Using equation (21) the average normal rotation along the side can be expressed in terms of the normal deflections as

$$\theta_{n_{jk}}^{(p)} = \tfrac{1}{2}(\boldsymbol{\lambda}_{jk}^{(p)} \boldsymbol{\nabla}' w'^{(p)} + \boldsymbol{\lambda}_{jk}^{(b)} \boldsymbol{\nabla}' w'^{(b)}) \tag{26}$$

where

$$\boldsymbol{\lambda}_{jk}^{(p)} = [-s_{jk}^{(p)}, c_{jk}^{(p)}] \tag{27}$$

Substituting equations (21) and (26) into (22) and choosing a standard linear interpolation for the displacement field within each triangle, the curvatures within element p can be expressed in terms of the normal deflection values of the patch nodes as:

$$\boldsymbol{\kappa}'_p = \mathbf{S}_p \mathbf{w}'_p \tag{28}$$

$$\mathbf{S}_p = [\mathbf{S}_{ij}^{(p)}, \mathbf{S}_{jk}^{(p)}, \mathbf{S}_{ki}^{(p)}] \tag{29}$$

$$\mathbf{w}'_p = [w'^{(p)}_i, w'^{(p)}_j, w'^{(p)}_k, w'^{(a)}_j, w'^{(a)}_i, w'^{(a)}_l, w'^{(b)}_k, w'^{(b)}_j, w'^{(b)}_m, w'^{(c)}_i, w'^{(c)}_k, w'^{(c)}_n]^{\mathrm{T}} \tag{30}$$

The explicit form of the different $\mathbf{S}_{ij}^{(p)}$ curvature matrices is given by Oñate and Zárate (2000). Note also that the definition of vector $\mathbf{w}'_p$ depends on the convention chosen for the local and global node numbers for the element patch (Figure 3).

The normal nodal deflections are related to the global nodal displacements by the following transformation

$$\mathbf{w}'_p = \mathbf{C}_p \mathbf{a}_p \tag{31}$$

where

$$\mathbf{C}_p = \begin{pmatrix} i & j & k & l & m & n \\ C_i^{(p)} & 0 & 0 & 0 & 0 & 0 \\ 0 & C_i^{(p)} & 0 & 0 & 0 & 0 \\ 0 & 0 & C_i^{(p)} & 0 & 0 & 0 \\ 0 & C_i^{(a)} & 0 & 0 & 0 & 0 \\ C_i^{(a)} & 0 & 0 & 0 & 0 & 0 \\ 0 & 0 & 0 & C_i^{(a)} & 0 & 0 \\ 0 & 0 & C_i^{(b)} & 0 & 0 & 0 \\ 0 & C_i^{(b)} & 0 & 0 & 0 & 0 \\ 0 & 0 & 0 & 0 & C_i^{(b)} & 0 \\ C_i^{(c)} & 0 & 0 & 0 & 0 & 0 \\ 0 & 0 & C_i^{(c)} & 0 & 0 & 0 \\ 0 & 0 & 0 & 0 & 0 & C_i^{(c)} \end{pmatrix} \qquad \mathbf{a}_p = \begin{Bmatrix} \mathbf{u}_i \\ \mathbf{u}_j \\ \mathbf{u}_k \\ \mathbf{u}_l \\ \mathbf{u}_{\mathrm{m}} \\ \mathbf{u}_n \end{Bmatrix} \tag{32}$$

with

$$\mathbf{C}_i^{(p)} = [c_{z'x'}^{(p)}, c_{z'y'}^{(p)}, c_{z'z'}^{(p)}] \qquad \mathbf{u}_i = \begin{Bmatrix} u_i \\ v_i \\ w_i \end{Bmatrix} \tag{33}$$

In this equation $c_{z'x}^{(p)}$ is the cosine of the angle between the local z' axis of element p and the global x axis, etc.

Substituting equation (31) into (27) finally gives

$$\boldsymbol{\kappa}_p' = \mathbf{B}_{\mathrm{b}_p} \mathbf{a}_p \tag{34}$$

where

$$\mathbf{B}_{\mathrm{b}_p} = \mathbf{S}_p \mathbf{C}_p \tag{35}$$

is the element curvature matrix. In this equation $\mathbf{a}_p$ is the vector containing the 18 nodal displacement variables of the six nodes belonging to the patch of elements associated to the pth triangle.

The bending stiffness matrix associated to the pth triangle is obtained by:

$$\mathbf{K}_{\mathrm{b}_p} = A^{(p)} \mathbf{B}_{\mathrm{b}_p}^{\mathrm{T}} \mathbf{D}_p \mathbf{B}_{\mathrm{b}_p} \tag{36}$$

2.1 Membrane stiffness matrix

The membrane contribution to the BST element is simply provided by the constant strain triangle (CST) under plane stress conditions.

The membrane stiffness matrix for the pth triangle is obtained as

$$\mathbf{K}_{\mathrm{m}_p} = A^{(p)} \mathbf{B}_{\mathrm{m}_p}^{T} \mathbf{D}_{\mathrm{m}} \mathbf{B}_{\mathrm{m}_p} \tag{37}$$

where $\mathbf{B}_{\mathrm{m}_p}$ is the membrane strain matrix associated to the pth triangle. Full details of the derivation of $\mathbf{B}_{\mathrm{m}_p}$ and equation (37) are given by Oñate and Zárate (2000).

2.2 BST element: full stiffness matrix and nodal force vector

The stiffness matrix for the BST element is obtained by adding the membrane and bending contributions, i.e.

$$\mathbf{K}_p = \mathbf{K}_{\mathrm{b}_p} + \mathbf{K}_{\mathrm{m}_p} \tag{38}$$

Recall that the dimensions of the stiffness matrix $\mathbf{K}_p$ is 18×18 as it links the 18 displacements of the six nodes contributing to the stiffness of the pth triangle. The assembly of the stiffness matrices $\mathbf{K}_p$ into the global equation system follows the standard procedure, i.e. a control domain is treated as a macro-triangular element with six nodes.

Note that the lack of rotational degrees of freedom eliminates the inconsistencies between the approximations of the displacement and rotation fields usual in folded thin shell elements (Zienkiewicz and Taylor, 2000).

The accuracy of the element in membrane dominated problems is obviously limited by the linear approximation chosen for the displacement field. This, however, suffices to provide very accurate results for non-linear dynamic problems as shown in the examples presented in Section 2.3. An enhanced membrane formulation for the BST element is described by Flores and Oñate (2001).

The equivalent nodal force vector is obtained similarly as for standard C^0 shell triangular elements (Zienkiewicz and Taylor, 2000). Thus, the contribution of a uniformly distributed load over an element is split into three equal parts among the three element nodes. As usual nodal point loads are directly assigned to a node.

2.3 Boundary conditions

The prescription of the displacement boundary conditions is a simple process as the side rotations are formulated in terms of the normal and tangential rotation values. This allows us to treat naturally all boundary condition types found in practice.

Note that, the conditions on the normal rotations are introduced when building up the curvature matrix, whereas the conditions on the nodal displacements and the tangential rotations are prescribed at the solution equation level.

Full details of the treatment of the boundary conditions in the BST element are given by Oñate and Zárate (2000) and Flores and Oñate (2001). As an example the case of a clamped edge is briefly described next.

2.3.1 Clamped edge ($\boldsymbol{u}_{\mathrm{i}} = \boldsymbol{u}_{\mathrm{j}} = \theta_{\mathrm{n_{ij}}} = \theta_{\mathrm{s_{ij}}} = 0$). The condition $\mathbf{u}_i = \mathbf{u}_j = 0$ is prescribed when solving the global system of equations. The condition $\theta_{\mathrm{s}_{ij}} = 0$ is automatically satisfied by prescribing the side displacements to a zero value.

The condition $\theta_{\mathrm{n}_{ij}} = 0$ is imposed by neglecting the terms contributed by $\theta_{\mathrm{n}_{ij}}$ in matrix $\mathbf{S}_b$ of equation (29).

Note that the central triangle in this case has the element adjacent to the boundary side missing (Figure 6). This has to be properly taken into account in the stiffness assembly process.

For further details on the treatment of the boundary conditions in the BST element see Oñate and Zárate (2000) and Flores and Oñate (2001).

Examples of the good behavior of the BST element for quasistatic linear and non-linear analysis of plates and shells are presented by Oñate and Zárate (2000) and Flores and Oñate (2001).

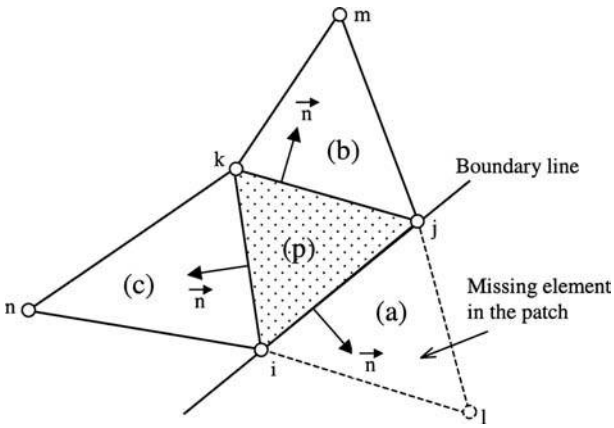

Figure 6.
Basic shell triangle next to a boundary line

3. Non-linear explicit dynamic formulation

The virtual work expression for the shell dynamics using an updated Lagrangian description is written as (Zienkiewicz and Taylor, 2000)

$$\int_{t_V} \delta\mathbf{u}^{\mathrm{T}} \rho \ddot{\mathbf{u}}\, \mathrm{d}V + \int_{t_V} \delta\mathbf{e}^{\mathrm{T}} \sigma\, \mathrm{d}V - \int_{t_\Gamma} \delta\mathbf{u}^{\mathrm{T}} \mathbf{q}\, \mathrm{d}\Gamma = 0 \tag{39}$$

where $\mathbf{u}$ and $\ddot{\mathbf{u}}$ are the nodal displacements and nodal accelerations, respectively, σ is the Cauchy stress vector, $\mathbf{e}$ is the Almansi strain vector, $\mathbf{q}$ is the surface load vector, V and Γ are, respectively, the volume and surface of the structure and ρ is the material density (assumed to be constant).

Discretization of equation (39) using the rotation-free BST formulation described in Section 2 gives

$$\mathbf{M}\ddot{\mathbf{a}} + \mathbf{p} = \mathbf{f} \tag{40}$$

where $\ddot{\mathbf{a}}$ is the vector of nodal displacement accelerations, $\mathbf{M}$ is the mass matrix, assumed here to be *lumped* at the nodes, and $\mathbf{p}$ and $\mathbf{f}$ are the internal and external nodal force vectors, respectively. Matrix $\mathbf{M}$ and vectors $\mathbf{p}$ and $\mathbf{f}$ are assembled from the element contributions, given for the BST element by:

$$\mathbf{M} = \rho \frac{A_p h_p}{3} \begin{bmatrix} \mathbf{I}_3 & & & \mathbf{0} & & \\ & \mathbf{I}_3 & & & & \\ & & \mathbf{I}_3 & & & \\ & & & \mathbf{0}_3 & & \\ & \mathbf{0} & & & \mathbf{0}_3 & \\ & & & & & \mathbf{0}_3 \end{bmatrix} \quad \mathbf{0}_3 = \begin{bmatrix} & 0 & & \\ & & & \mathbf{0} \\ & & 0 & \\ \mathbf{0} & & & \\ & & & 0 \end{bmatrix} \tag{41}$$

$$\mathbf{p} = \mathbf{B}^{\mathrm{T}} \left[\int_{-h_p/2}^{+h_p/2} \mathbf{S}^{\mathrm{T}} \boldsymbol{\sigma}'\, \mathrm{d}h \right] A_p \tag{42}$$

$$\mathbf{f} = \frac{A_p}{3} [\mathbf{q}^{\mathrm{T}}, \mathbf{q}^{\mathrm{T}}, \mathbf{q}^{\mathrm{T}}, \mathbf{0}, \mathbf{0}, \mathbf{0}]^{\mathrm{T}} \tag{43}$$

Equation (42) is integrated across the thickness by considering a number of layers with uniform material properties each. The strain matrix $\mathbf{B}$ in equation (42) contains the bending and membrane contributions to the triangle, i.e.

$$\mathbf{B} = \begin{Bmatrix} \mathbf{B}_{\mathrm{m}} \\ \mathbf{B}_{\mathrm{b}} \end{Bmatrix}$$

Matrix $\mathbf{S}$ in equation (42) is given by:

$$\mathbf{S} = \begin{bmatrix} 1 & 0 & 0 & z' & 0 & 0 \\ 0 & 1 & 0 & 0 & z' & 0 \\ 0 & 0 & 1 & 0 & 0 & z' \end{bmatrix} \tag{44}$$

Finally, vector $\boldsymbol{\sigma}'$ denotes the stresses defined in local axes, i.e. $\boldsymbol{\sigma}' = [\sigma_{x'}, \sigma_{y'}, \sigma_{x'y'}]^{\mathrm{T}}$

The constitutive model is based on a standard hypoelastic law defining the (objective) stress rate as

$$\mathring{\sigma}_{ij} = D_{ijkl}(d_{kl} - d^{p}_{kl}) \tag{45}$$

where $\mathbf{D}$ is the fourth order elastic constitutive tensor taken here to be equal to that of infinitesimal elasticity, d_{ij} is the symmetric part of the strain rate tensor defined as

$$\mathrm{d}_{ij} = \frac{1}{2}\left(\frac{\partial \dot{u}_i}{\partial x_j} + \frac{\partial \dot{u}_j}{\partial x_i}\right) \tag{46}$$

and d^{p}_{ij} is the plastic part of d_{ij} defined by the following flow rule

$$d^{p}_{kl} = \lambda \frac{\partial f}{\partial \sigma_{kl}} \tag{47}$$

where $f(\boldsymbol{\sigma}, \mathbf{q})$ is the yield function and $\mathbf{q}$ represent the internal parameters.

The objective derivatives $\mathring{\sigma}_{ij}$ are defined here by the Jaumann stress rate giving

$$\mathring{\sigma}_{ij} = \dot{\sigma}_{ij} - w_{ip}\sigma_{jp} + \sigma_{pj}w_{ip} \tag{48}$$

where the spin tensor w_{ij} is defined as:

$$w_{ij} = \frac{1}{2}\left(\frac{\partial \dot{u}_i}{\partial x_j} - \frac{\partial \dot{u}_j}{\partial x_i}\right) \tag{49}$$

It is well known that the use of the Jaumann stress rate with kinematic strain hardening can lead to spurious oscillations under pure shear states (Dienes, 1979). This defect can be avoided by using the Green–Naghdi stress rate for kinematic strain-hardening situations. This introduces some additional complexity in the analysis as the Green–Naghdi stress rate requires the

evaluation of the rotation tensor. Alternatively, a hyperelastic constitutive model can be used (Crisfield, 1997).

The use of hypoelastic models has also been critisized as they dissipate elastic energy in pure elastic problems. This defect has little consequences in elasto-plastic problems (Crisfield, 1997).

4. Explicit time integration

The explicit time integration algorithm follows the classical steps described below.

(1) The nodal accelerations are explicitly computed by

$$\ddot{\mathbf{a}}^n = \mathbf{M}^{-1}[\mathbf{f}^n - \mathbf{p}^n] \tag{50}$$

where $(\cdot)^n$ denotes values at time $t = t_n$.

(2) The nodal velocities are computed at $t^n + \Delta t^n/2$ by:

$$\dot{\mathbf{a}}^{n+1/2} = \dot{\mathbf{a}}^{n-1/2} + \mathbf{a}^n \Delta t^n \tag{51}$$

(3) The global displacements are computed at t^{n+1} by:

$$\mathbf{a}^{n+1} = \mathbf{a}^n + \dot{\mathbf{a}}^{n+1/2} \Delta t^{n+1/2} \tag{52}$$

(4) The geometry is updated by

$$\mathbf{x}^{n+1} = \mathbf{x}^n + \Delta \mathbf{a} \tag{53}$$

with

$$\Delta \mathbf{a} = \mathbf{a}^{n+1} - \mathbf{a}^n \tag{54}$$

(5) The constitutive equation is integrated for each element in the mesh following the next steps:

(5.1) The local nodal displacements for an element p are computed by

$$\Delta \mathbf{a}'_p = \mathbf{T}_p \Delta \mathbf{a}_p \tag{55}$$

where matrix $\mathbf{T}_p$ transforms the global nodal displacements of the element to the local coordinate system (Oñate and Zárate, 2000).

(5.2) The new element area is computed as A_p^{n+1} and the element thickness is updated to ensure incompressible behavior. This gives:

$$h_p^{n+1} = \frac{(A_p h_p)^n}{A_p^{n+1}} \tag{56}$$

(5.3) The increment of local strains is computed for the ith material layer across the thickness as

$$\Delta\boldsymbol{\varepsilon}' = [\mathbf{B}'_m + z'_i\mathbf{B}'_b]^{n+1/2}\Delta\mathbf{a}'_p \tag{57}$$

where z'_i is the thickness coordinate of the ith layer.

(5.4) The elastic Jaumann stress are predicted by

$$\boldsymbol{\sigma}'^{n+1/2} = \boldsymbol{\sigma}'^{n} + \mathring{\boldsymbol{\sigma}}'^{n+1/2}\Delta t + [\mathbf{W}^{n+1/2}\sigma'^{n} - \boldsymbol{\sigma}'^{n}\mathbf{W}^{n+1/2}]\frac{\Delta t}{2} \tag{58}$$

where $\mathbf{W}$ is the spin tensor matrix,

$$\mathring{\sigma}'^{n+1/2} = \mathbf{D}\mathbf{d}^{n+1/2} \tag{59}$$

and

$$\mathbf{d}^{n+1/2} = \frac{2\Delta\boldsymbol{\varepsilon}'}{\Delta t} \tag{60}$$

in equation (59) $\mathbf{D}$ is the elastic constitutive matrix.

(5.5) The yield criterion is checked

$$\text{IF} \quad f(\boldsymbol{\sigma}'^{n+1/2}, \boldsymbol{\alpha}^{n+1/2}) > 0$$

$$\text{THEN go to 5.6}$$

$$\text{ELSE go to 5.7}$$

where f is the yield function and $\boldsymbol{\alpha}$ are internal variables of the constitutive model.

(5.6) The stresses are *corrected* using a radial return algorithm (Zienkiewicz and Taylor, 2000; Crisfield, 1997)

(5.7) The local stresses $\boldsymbol{\sigma}'^{n+1/2}$ are transported to the configuration at time $n+1$

$$\boldsymbol{\sigma}'^{n+1} = \boldsymbol{\sigma}'^{n+1/2} + [\mathbf{W}\boldsymbol{\sigma}' - \boldsymbol{\sigma}'\mathbf{W}]^{n+1/2}\frac{\Delta t}{2} \tag{61}$$

(6) The steps (5.2)–(5.7) are repeated for each layer. Next the local internal force vector for the pth element is computed by integrating equation (42) over the number of material layers chosen as:

$$\mathbf{p}_p'^{n+1} = A_p^{n+1} \sum_{i=1}^{\text{nlayers}} [\mathbf{B}_m' + z_i' \mathbf{B}_b^{T'}]^{n+1} \boldsymbol{\sigma}'^{n+1} \Delta z_i' \tag{62}$$

(7) The local internal force vector for the element is transformed to global cartesian axes by

$$\mathbf{p}_p^{n+1} = [\mathbf{T}_p^T]'^{n+1} \mathbf{p}_p'^{n+1} \tag{63}$$

The global internal force vectors for the different elements are subsequently assembled into the global vector $\mathbf{p}^{n+1}$.

(8) The external forces at time t^{n+1} are computed. The effect of frictional contact forces is taken into account at this step for the computation of $\mathbf{f}^{n+1}$.

(9) The process is restarted at step 1 for the computation of the nodal accelerations at t^{n+1}.

The performance of the BST element for structural dynamic analysis using the explicit integration scheme presented earlier is shown next in some examples of application.

5. Examples

5.1 Example 1. Clamped spherical dome under impulse pressure loading

The geometry of the dome and the material properties chosen are shown in Figure 7. A uniform pressure load of 600 psi is applied to the upper surface of the dome. The different meshes used in the analysis are shown in Figure 8. One-fourth of the dome is considered only due to symmetry. Two different analyses under elastic and elasto-plastic conditions were carried out.

Figure 9 shows results for the time history of the central deflection using different meshes and *elastic material properties*. Results obtained with the BST element for mesh 3 of Figure 10 are compared with those obtained with the DKT-15 shell element (combining the standard d.o.f. DKT plate element (Batoz *et al.*, 1980) and the 6 d.o.f. constant strain triangle (Zienkiewicz and Taylor, 2000)) using mesh 2 involving 1219 d.o.f. and with explicit results reported by WHAMS-3D and the implicit FE solution given by Bathe *et al.* (1975). Note the accuracy of the BST element for a relatively simple mesh.

Figure 11 shows the evolution of the *elastoplastic material solution* with the number of thickness layers in equation (62) using the BST element and mesh 2. Note that four layers suffice to provide an accurate solution.

Figure 12 compares the time evolution of the central displacement obtained with the BST element (mesh C) for an *elasto-plastic material* with similar results

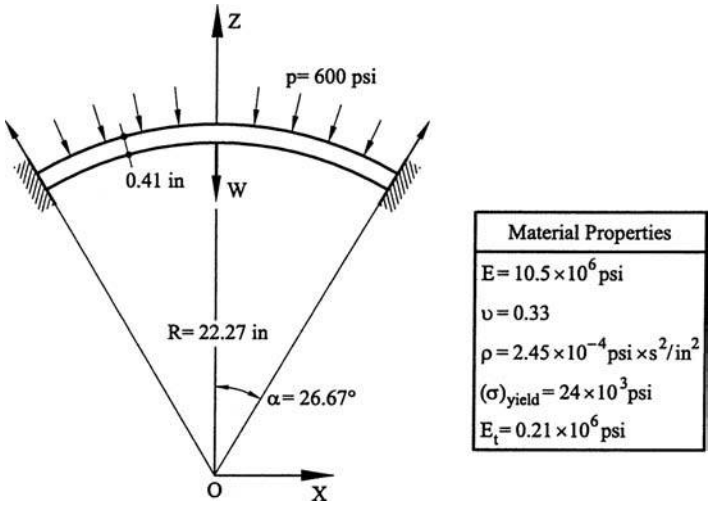

Figure 7.
Spherical dome. Geometry, loading and material properties

obtained with the DKT-15 element and reported by Bathe *et al.* (1975) and WHAMS-3D. The good performance of the BST element is again noticeable.

The deformed shapes of the dome at different times are shown in Figure 13. A summary of results for the central deflection at significant times is given in Tables I and II. Further details on the solution of this problem with the BST element are reported by Cendoya *et al.* (1997).

5.2 Example 2. Cylindrical panel under impulse loading

The geometry of the cylinder and the material properties are shown in Figure 14. A prescribed initial vertical velocity of $v_0 = -5650\,\mathrm{m/s}$ is applied to the points in the region shown in Figure 14 modeling the effect of an impulse vertical load. One-half of the cylinder is discretized only due to symmetry conditions. Two different meshes of 6×12 and 12×32 BST elements were used for the analysis. The problem was also analyzed with the DKT-15 element using the same meshes. The different degrees of freedom involved in the analysis for each element and each of the two meshes is shown in Figure 15.

The analysis was performed assuming an elasto-perfect plastic material behavior. A study of the convergence of the solution with the number of thickness layers again showed that four layers suffice to capture accurately the non-linear material response.

Figures 16 and 17 show the time evolution of the vertical displacement of two reference points along the center line located at $z = -6.28\,\mathrm{in.}$ and $z = -9.42\,\mathrm{in.}$, respectively. Results of Figure 16 were obtained with the BST element, whereas those of Figure 17 were obtained with the DKT-15 element. Note the better convergence of the BST element for a considerably smaller

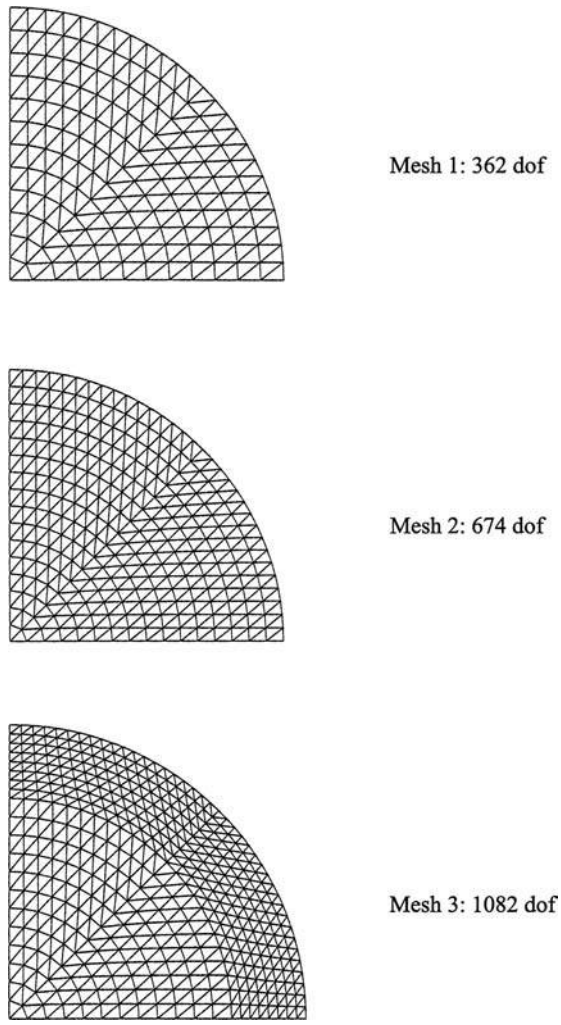

Figure 8.
Spherical dome. Meshes used in the analysis

number of elements. A comparison of the results obtained with both elements using the finer mesh is shown in Figure 18 where experimental results reported by Balmer and Witmer (1964) have also been plotted for comparison purposes. Good agreement between the numerical and experimental results is obtained.

The numerical values of the vertical displacement at the two reference points obtained with the BST and DKT-15 elements after a time of 0.4 ms using the 16×32 mesh are compared in Table III with experimental results and also with a numerical solution reported by Stolarski *et al.* (1984)) using a curved triangular shell element and the 16×32 mesh. It is interesting to note the

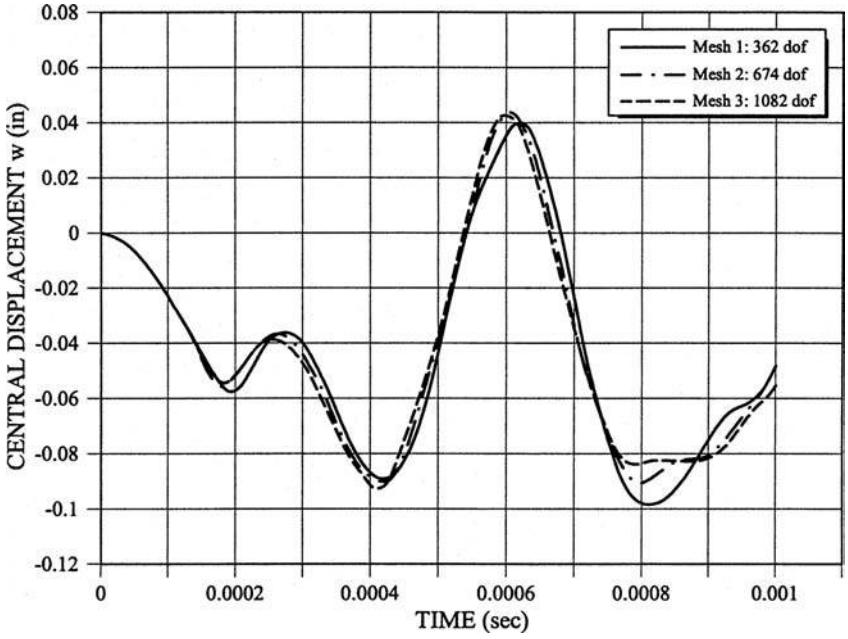

Figure 9.
Spherical dome. Linear elastic material. Convergence of the dynamic solution with the BST element using mesh 3 of Figure 8

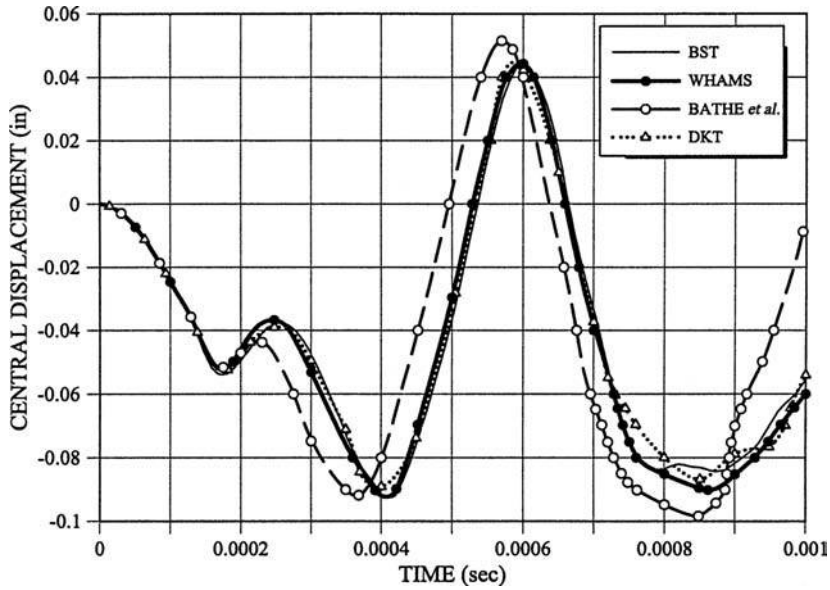

Figure 10.
Spherical dome. Linear elastic material. Comparison of results obtained with the BST element (mesh 3, 1082 d.o.f), the DKT15 element (Batoz *et al.*, 1980) (mesh 2, 1219 d.o.f.) and alternative explicit (WHAMS-3D) and implicit (Bathe *et al.*, 1975) solutions

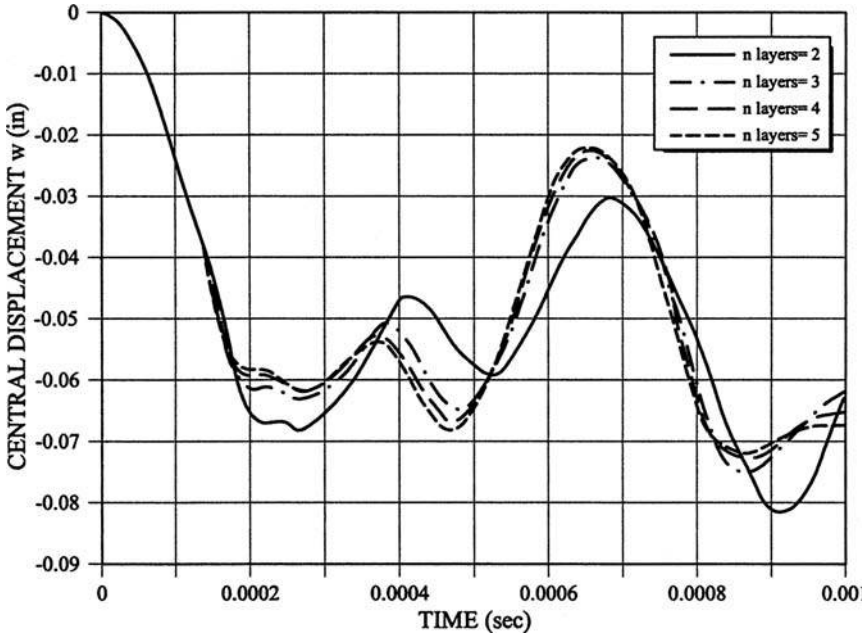

Figure 11.
Spherical dome. Elasto-plastic material. Results obtained with the BST element (mesh 2) using different layers for the thickness integration of stresses

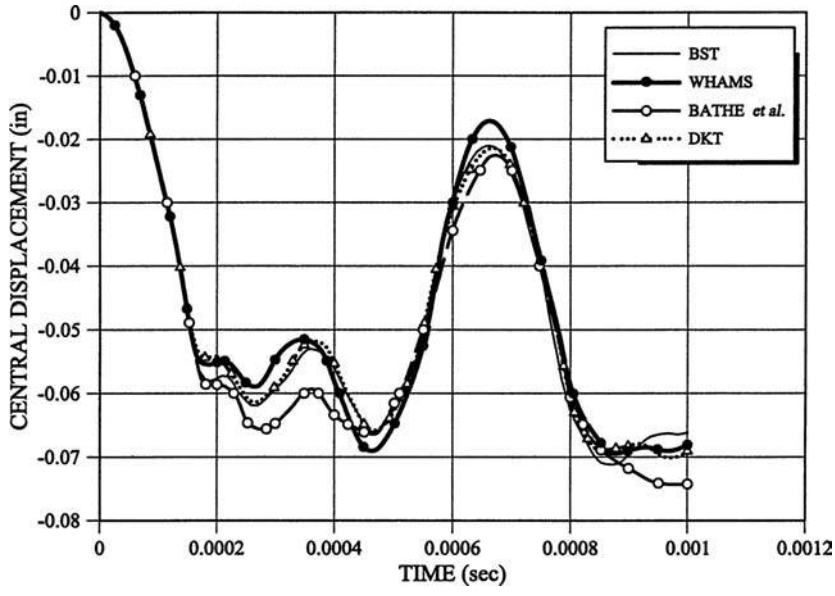

Figure 12.
Spherical dome. Elasto-plastic material. Comparison of results obtained with the BST element (mesh 3, 1082 d.o.f), the DKT15 element (Batoz *et al.*, 1980) (mesh 2, 1219 d.o.f) and alternative explicit (WHAMS-3D) and implicit (Bathe *et al.*, 1975) solutions

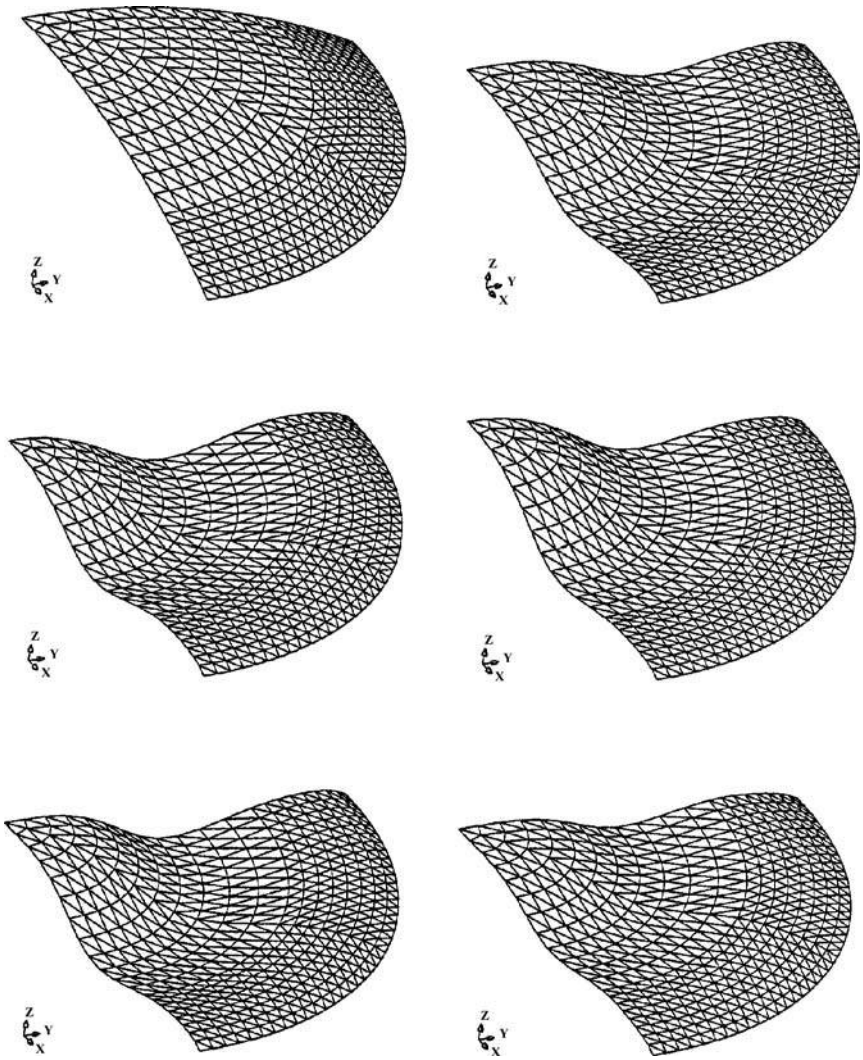

Figure 13.
Spherical dome. Elasto-plastic material. Deformed shapes at different times, $t = 0$, 0.2, 0.4, 0.6, 0.8 and 1.0 ms

Table I.
Spherical dome. Elastic material. Comparison of the central deflection values at the mid point obtained with the BST element and others

	Central deflection (in.)		
	$t = 0.2$ ms	$t = 0.4$ ms	$t = 0.6$ ms
BST	− 0.0500	− 0.0915	0.0435
DKT15	− 0.0475	− 0.0918	0.0420
WHAMS-3D	− 0.0466	− 0.0905	0.0457
Bathe *et al.* (1975)	− 0.0466	− 0.0800	0.0457

accuracy of all results for $z = -6.28$ in. and the uniform discrepancy of all numerical solutions with the experimental value for $z = -9.42$ in.

The deformed shapes of the transverse section for $z = -6.28$ in. and the longitudinal section for $x = 0$ obtained with the BST element (finer mesh) after 1 ms are compared with the experimental results in Figure 19. Good agreement is again observed.

Finally, the deformed mesh of 12×32 BST elements is plotted in Figure 20.

5.3 Example 3. Impact between two tubes

The geometry of the two tubes before the impact and the elasto-perfect-plastic material properties are shown in Figure 21. The impact velocity is $v_0 = 30$ m/s. A mesh of 300 BST elements (990 d.o.f.) was used to discretize each tube as

Table II.
Spherical dome. Elasto-plastic material. Comparison of the central deflection values at the mid point obtained with the BST element and others

	Central deflection (in.)		
	$t = 0.2$ ms	$t = 0.4$ ms	$t = 0.6$ ms
BST	− 0.0576	− 0.0562	− 0.0300
DKT15	− 0.0547	− 0.0576	− 0.0290
WHAMS-3D	− 0.0543	− 0.0571	− 0.0314
Bathe *et al.* (1975)	− 0.0580	− 0.0619	− 0.0361

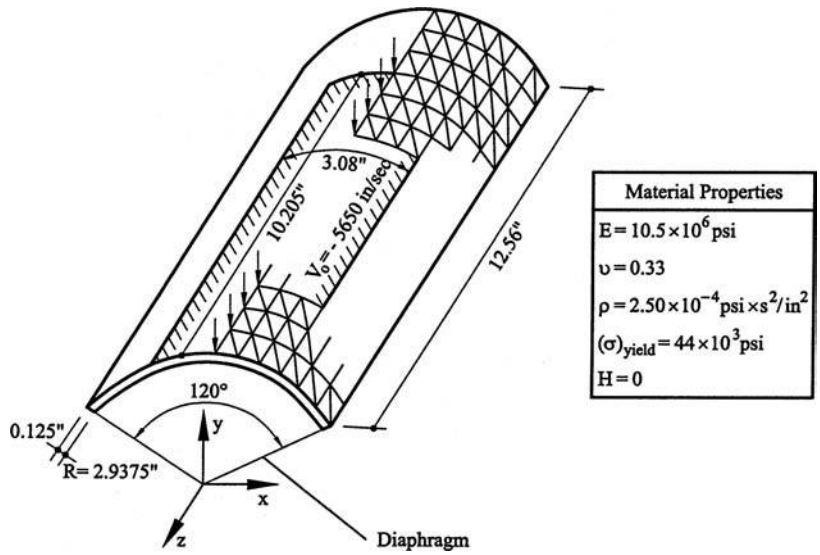

Figure 14.
Cylindrical panel under impulse loading. Geometry, prescribed velocity conditions and material properties

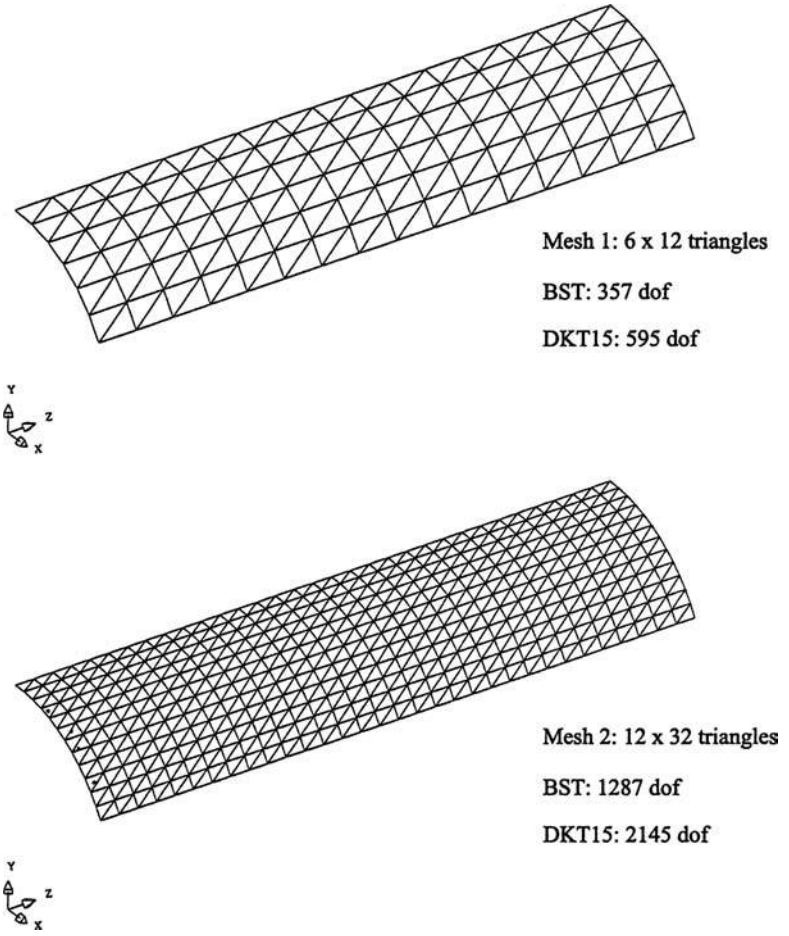

Figure 15.
Cylindrical panel. Meshes used in the analysis with BST and DKT15 elements. The d.o.f. involved for each element are shown

shown in Figure 22. The problem was also analyzed using a regular mesh of 10×15 four-node shell quadrilaterals (1650 d.o.f.) based on Reissner–Mindlin theory and an assumed transverse shear strain field (Simo *et al.*, 1990).

Figure 23 shows the time evolution of the horizontal displacement of node 171 diametrically opposed to the node of initial contact (see Figure 21). Numerical results obtained with the two elements mentioned earlier are compared with those obtained by Zhong (1993) using a mesh of 300 four-noded bilinear shell elements and also with the results from the 10×15 mesh of four node assumed shear strain quadrilaterals (Simo *et al.*, 1990). Note the excellent performance of the BST element for a considerably less number of degrees of freedom.

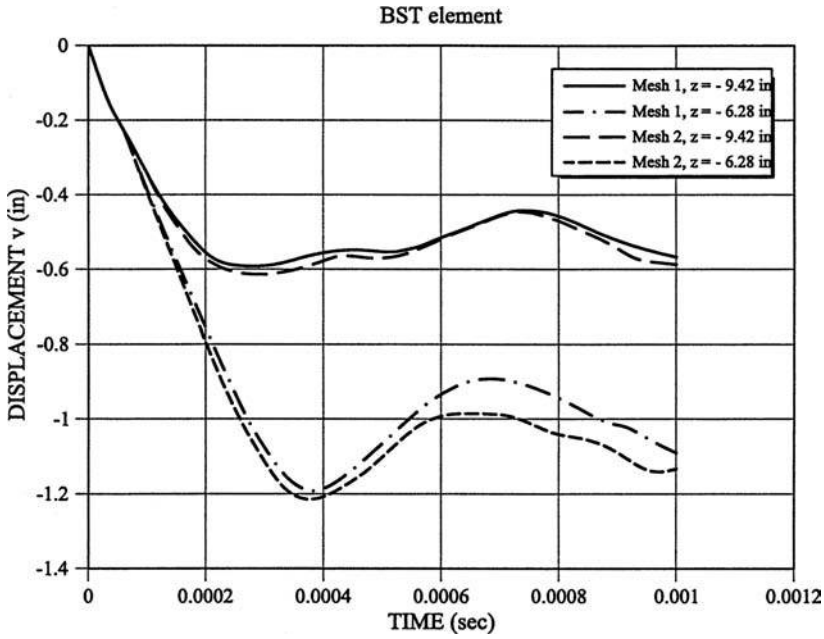

Figure 16.
Cylindrical panel. Time evolution of the vertical displacement of two points along the central line for $z = -6.28$ in. and $z = -9.42$ in. Results obtained using the BST element and mesh 2 of Figure 15

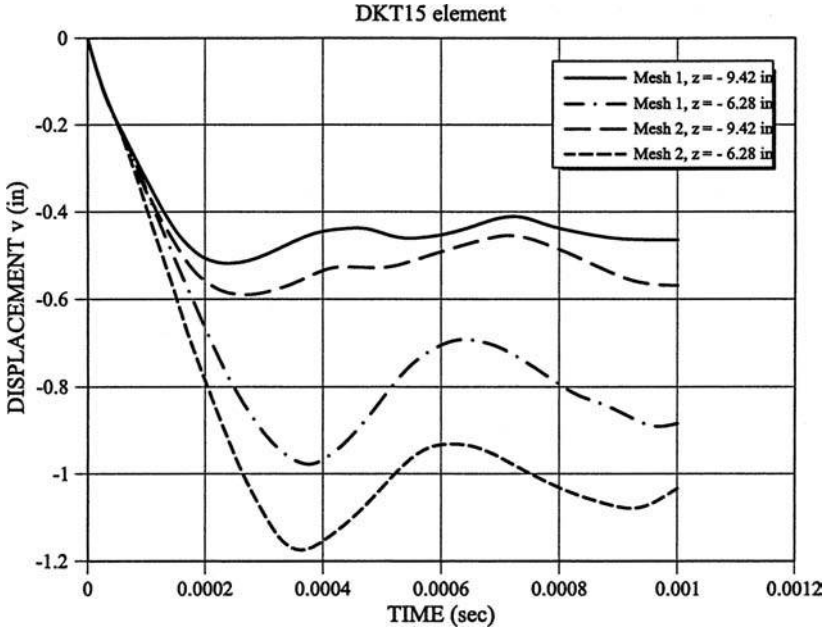

Figure 17.
Cylindrical panel. Time evolution of the vertical displacement of two points along the central line for $z = -6.28$ in. and $z = -9.42$ in. Results obtained using the DKT15 element and mesh 2 of Figure 15

The geometry of the two tubes at different times after the impact are shown in Figure 24.

5.4 Example 4. Stretch forming of a hemispherical cup

Figure 25 shows the geometry of the circular sheet, the hemispherical punch and the die region. The sheet is deformed into a cup by frictional contact with the punch and the die. The material properties for this problem can be seen in Table IV. A simple discretization of the sheet into 184 BST elements was used for the analysis as shown in Figure 25. Both the punch and the die were discretized with rigid triangles. A Coulomb friction model was used to simulate frictional conditions between the sheet and the forming tools.

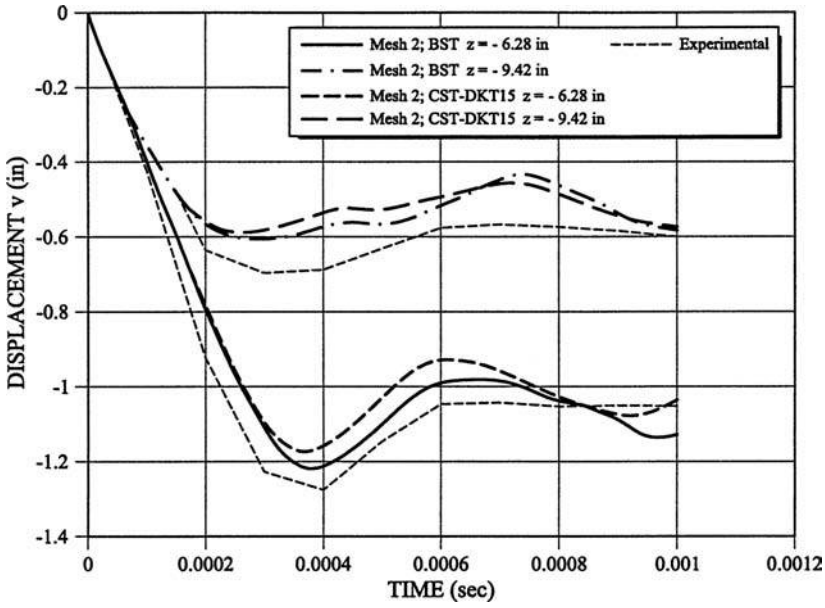

Figure 18. Cylindrical panel. Time evolution of the vertical displacement of two points along the central line for $z = -6.28$ in. and $z = -9.42$ in. Comparison of results obtained with the BST and DKT15 elements using mesh 2 of Figure 15. Experimental results reported by Balmer and Witmer (1964) are also plotted

	Vertical displacement (in.)	
	$z = -6.28$ in.	$z = -9.42$ in.
BST (12×32el.)	− 1.213	− 0.574
KT15 (12×32el.)	− 1.160	− 0.553
Stolarski *et al.* (1984)	− 1.183	− 0.530
Experimental Stolarski *et al.* (1984)	− 1.280	− 0.700

Table III. Cylindrical panel. Comparison of vertical displacement values of two central points for $t = 0.4$ ms

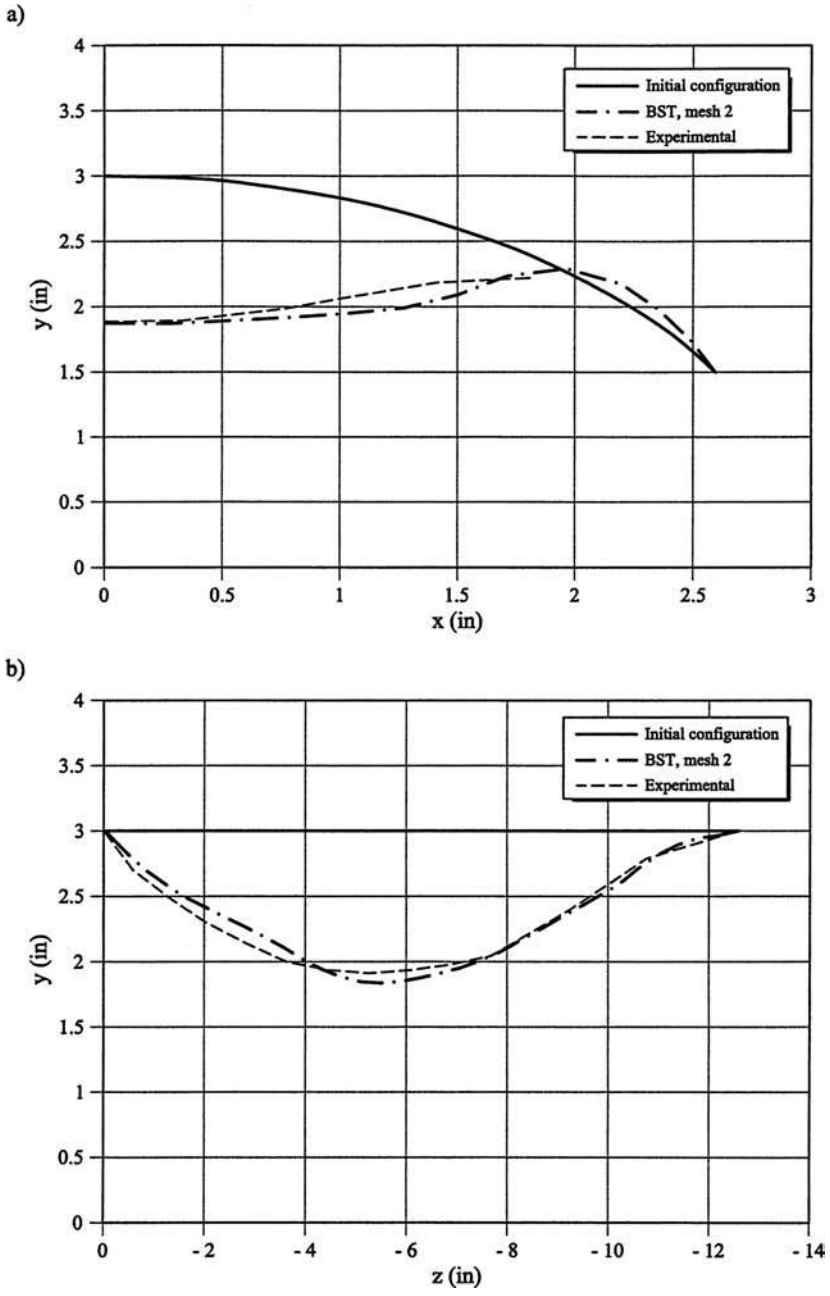

Figure 19.
Cylindrical panel. Deformed shapes after 1 ms obtained with the BST element (12×32 mesh) and experimentally. (a) Transverse section for $z = -6.28$ in. (b) Longitudinal section along the symmetry axis $x = 0$

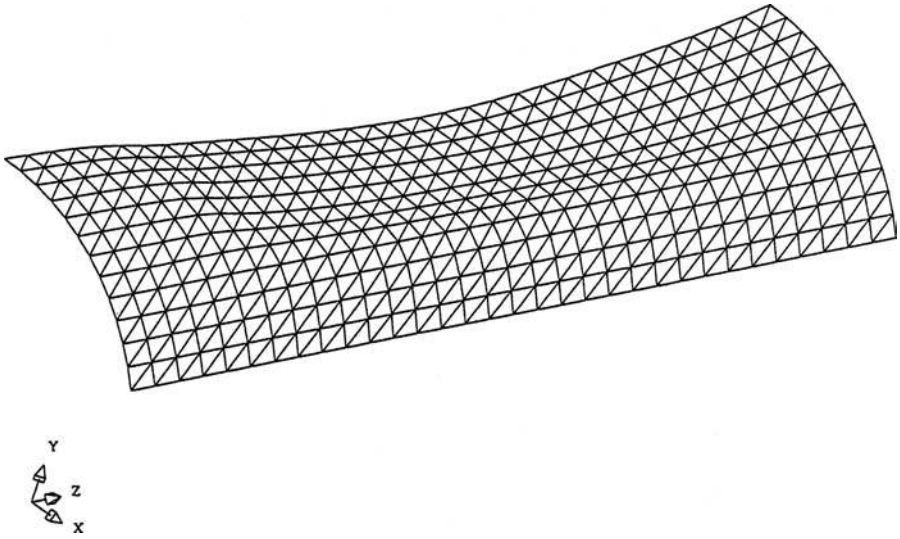

Figure 20.
Cylindrical panel. Deformed mesh of 12 × 32 BST element after 1 ms

Figures 26 and 27 show the distribution of the effective plastic strain ($\bar{\varepsilon} = 1/2(\varepsilon^p_{ij}\varepsilon^p_{ij})^{1/2}$) along a radial line for different punch travel distances and two friction coefficients of $f = 0.0$ and 0.30, respectively. Numerical results obtained with the BST element are compared with those obtained using four-node axysymmetric elasto-plastic solid quadrilateral elements (Garcúa, 1993) and by Agelet de Saracibar and Oñate (1991) using two-node axisymmetric viscous shell elements (Agelet de Saracibar and Oñate, 1991; Oñate and Agelet de Saracibar, 1991). Note the general agreement between all solutions.

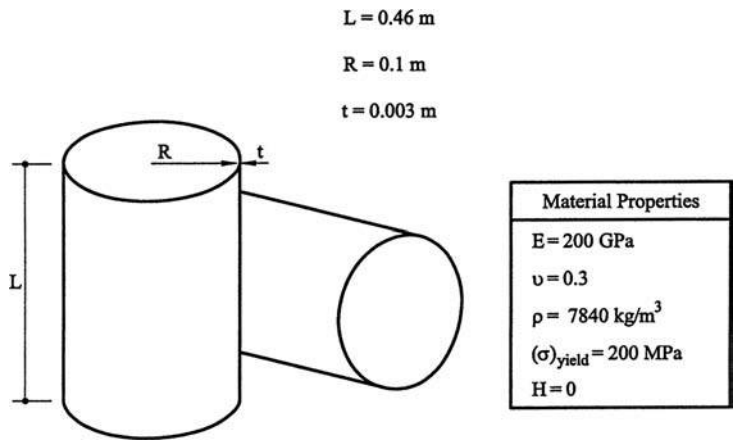

Figure 21.
Impact between two tubes. Geometry of the tubes and material properties

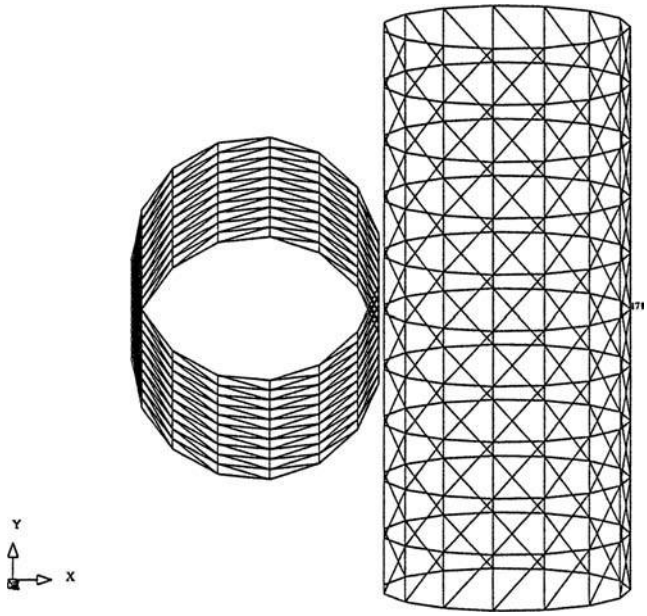

Figure 22.
Meshes of 300 BST elements used to discretize each tube

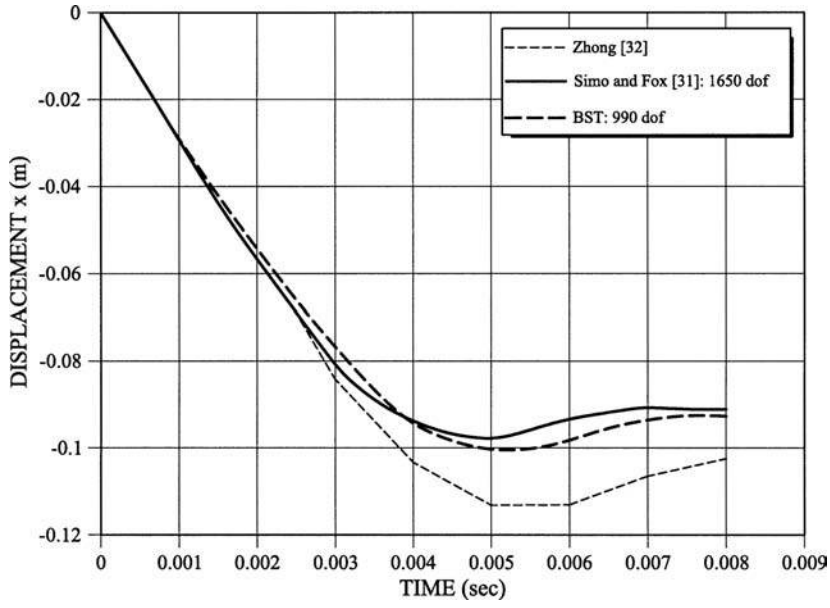

Figure 23.
Impact between two tubes. Time evolution of node 171 (see Figure 22)

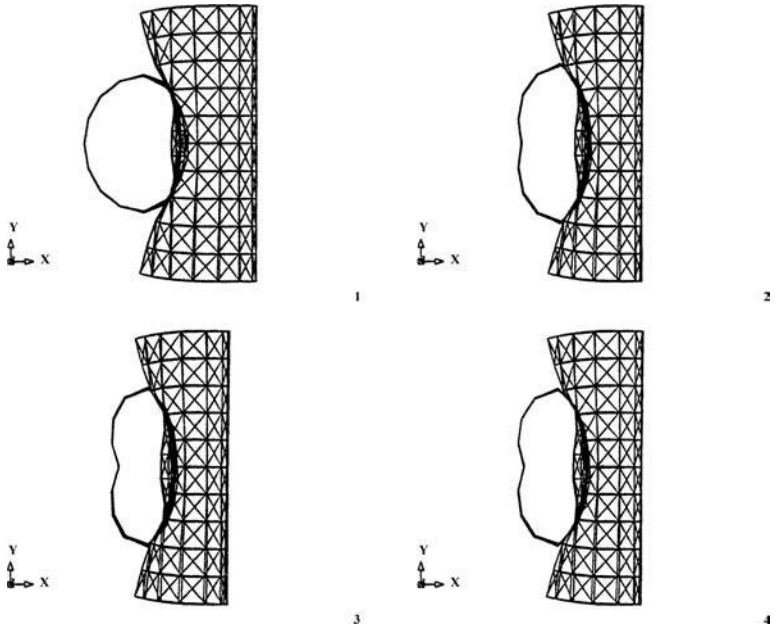

Figure 24.
Deformed shapes of the tubes after 2, 4, 6 and 8 ms obtained with the BST element

Numerical results obtained with the BST element for this problem also agrees well with experimental values reported in a benchmark test exercise for sheet forming analysis carried out at Ohio State University (Lee *et al.*, 1998).

5.5 Example 5. Deep drawing of a square box

This problem was part of an experimental–numerical benchmark exercise proposed at NUMISHEET'93 conference (1993). Details of the geometry of the steel sheet and the forming tools are shown in Figure 28. The anisotropic material properties are given in Table IV. Material anisotropy was treated using the Hill 48 model for normal anisotropy conditions (Hill, 1948).

The sheet geometry was discretized using 1800 BST elements (Figure 29). The different tools were modeled using rigid quadrilateral elements as shown in Figure 29.

Figures 30 and 31 show the distribution of the logarithmic thickness strain along lines OA and OB for a punch travel distance of 40 mm. Results obtained with the BST element are in agreement with those reported by other participants at NUMISHEET'93 using different codes (NUMISHEET'93 conference, 1993). The average of many experimental results reported at this meeting is also plotted in the figures for comparison purposes. There is good

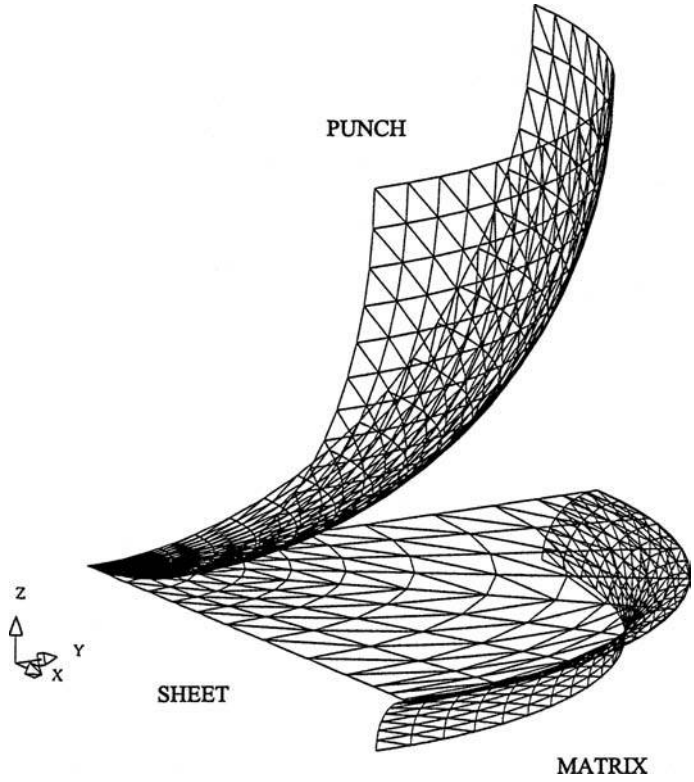

Figure 25.
Stretch forming of a hemispherical cup. Discretization of the sheet into 184 BST elements. The die and the punch are discretized using rigid triangles

Young's modulus	69 Gpa
Poisson coefficient	0.3
Density	2730 kg/m^3
1D stress–strain law	$\bar{\sigma} = 589(10^{-4} + \bar{\varepsilon}_p)^{0.216}$
Radius of sheet	59.18 mm
Sheet thickness	1.0 mm
Punch radius	50.8 mm
Die radius	6.35 mm
Punch speed	10 sin (500 t) mm/s
Time of analysis	6.28 ms
Coulomb friction coefficients	0.0 and 0.30

Table IV.
Stretch forming of a hemispherical cup. Geometry, material properties and process parameters

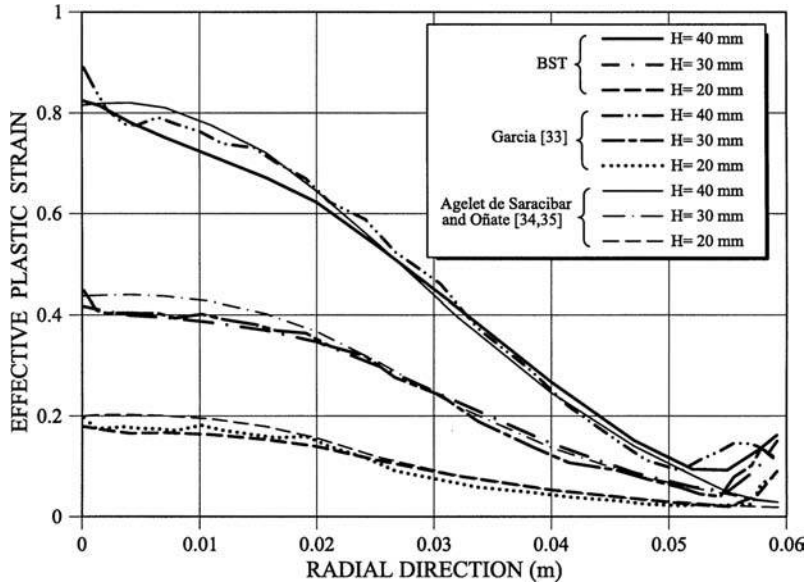

Figure 26.
Stretch forming of a hemispherical cup. Radial distribution of effective plastic strain values for punch travels of 20, 30, 40 mm and a friction coefficient of 0.0

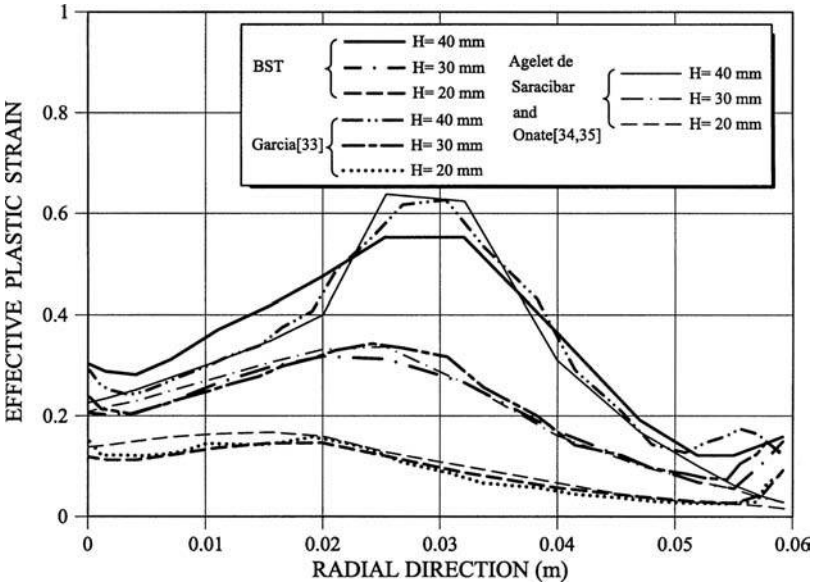

Figure 27.
Stretch forming of a hemispherical cup. Radial distribution of effective plastic strain values for punch travels of 20, 30, 40 mm and a frictional coefficient of 0.30

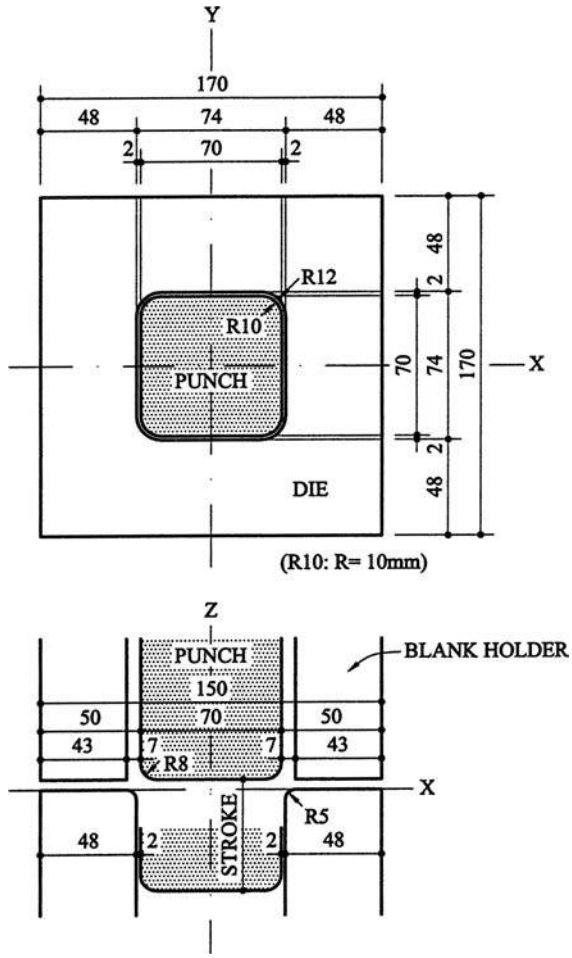

Figure 28.
Deep drawing of a square box. Definition of the geometry of the punch, the dies and the blank holder

agreement between results obtained with the relatively coarse mesh of BST element and the experimental values.

Figures 32 and 33 show, respectively, the distribution of the major and minor principal strains along the line OB obtained with the BST element. The, results agree well with those reported by participants at NUMISHEET'93 conference (1993).

A vertical view of the original and deformed sheet geometries (punch travel= 40 mm) is shown in Figure 34. A general perspective of the deformed sheet geometry and the distribution of effective plastic strain for $H = 40$ mm is shown in Figure 35.

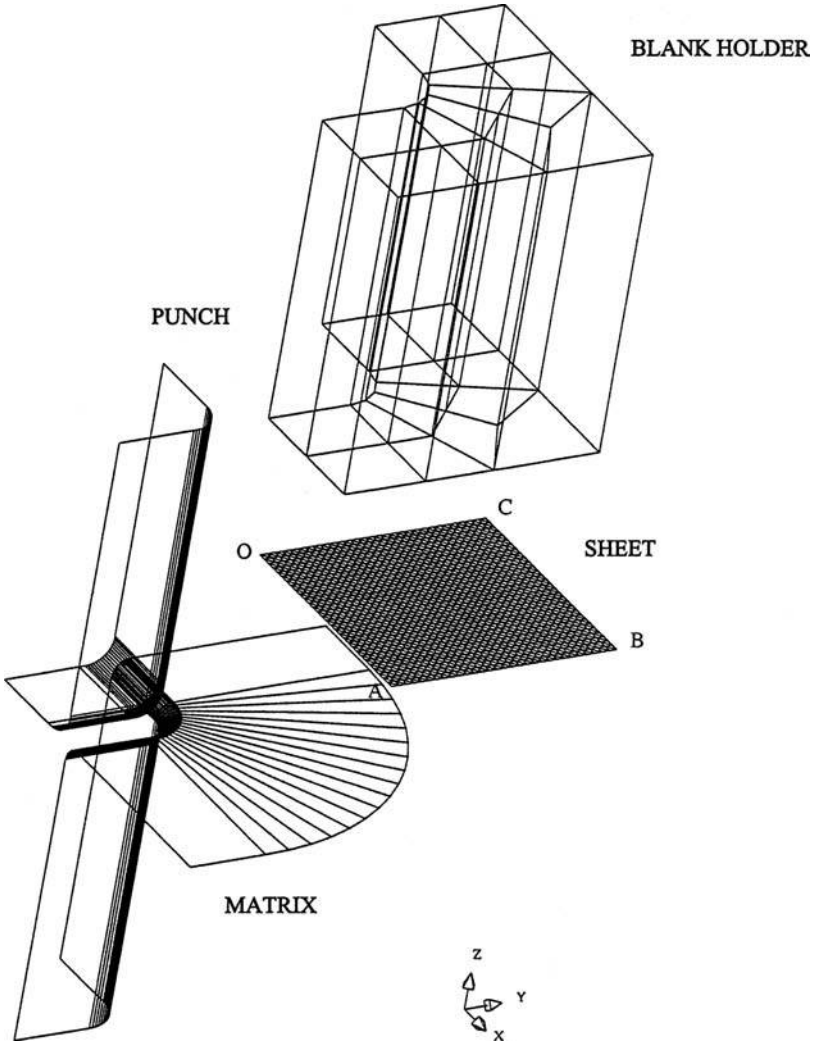

Figure 29.
Deep drawing of a square box. Discretization of the sheet into 1800 BST elements. The different tools are discretized using rigid elements

5.6 Example 6. Deep drawing of a curved rail

This problem was proposed as a benchmark in the NUMISHEET'96 conference (1996). A view of the discretization of the mild steel sheet into 1200 BST elements and the discretization of the different tools into rigid quadrilaterals can be seen in Figure 36. Details of the tools geometry, the material properties and the experimental and numerical results obtained in the benchmark exercise can be found in NUMISHEET'96 conference (1996)) Table V.

Figure 37 shows the final geometry of the sheet mesh for a punch travel distance of 37 mm obtained with the BST element superseded to the mesh

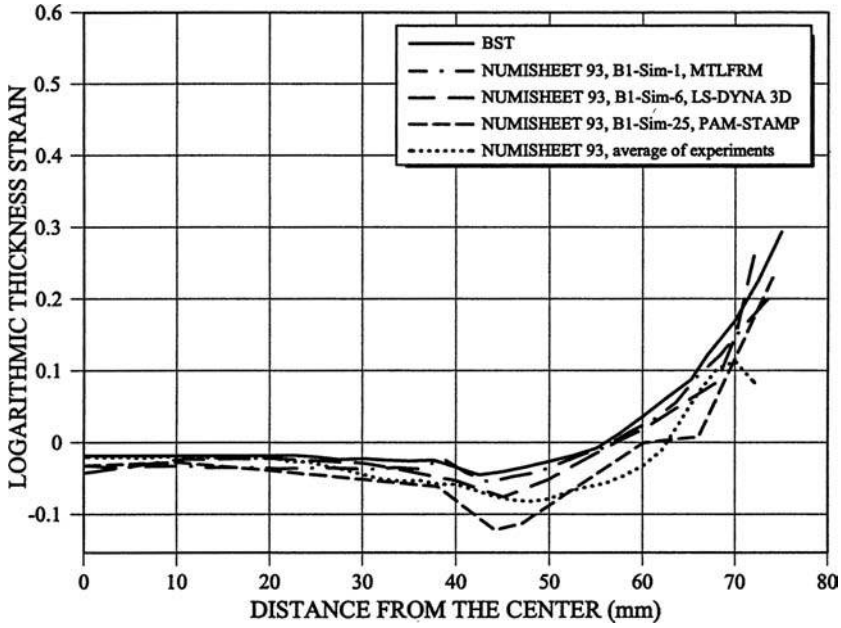

Figure 30.
Deep drawing of a square box. Distribution of logarithmic thickness strain ($\varepsilon_3 = \ln\ h/h_0$) along the line OA for a punch travel of 40 mm. Numerical results obtained with the BST element are compared with those reported in NUMISHEET'93 conference (1993)

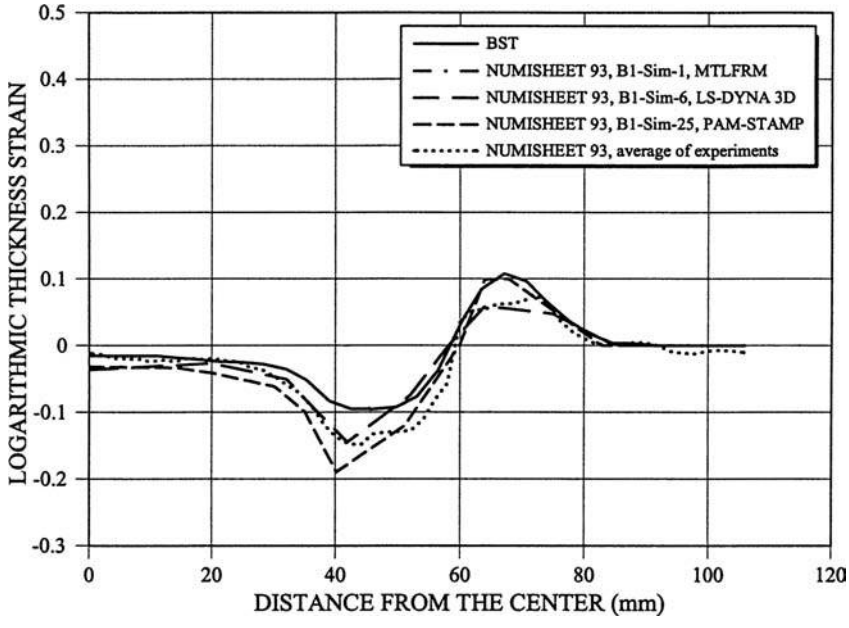

Figure 31.
Deep drawing of a square box. Distribution of logarithmic thickness strain ($\varepsilon_3 = \ln\ h/h_0$) along the line OB for a punch travel of 40 mm. Numerical results obtained with the BST element are compared with those reported in NUMISHEET'93 conference (1993)

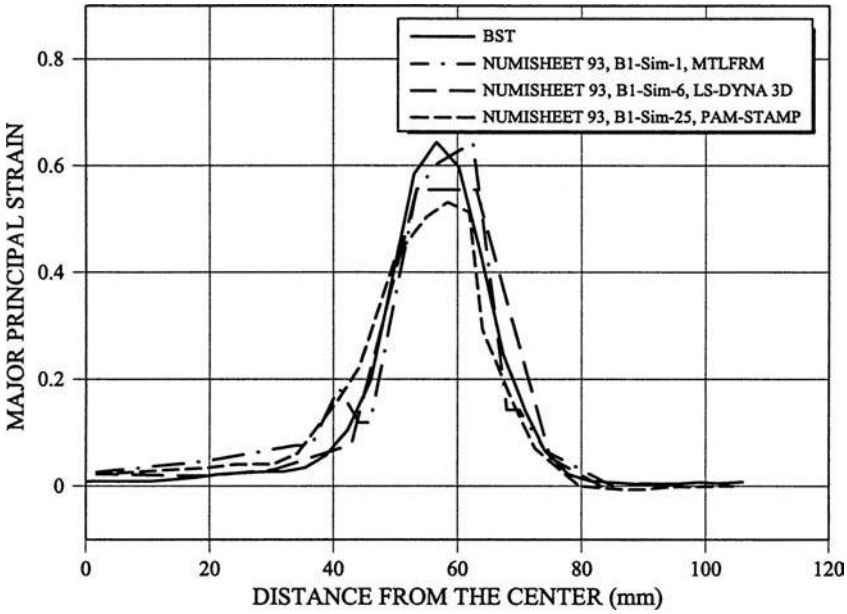

Figure 32.
Deep drawing of a square box. Distribution of major principal strain ε_1 along the line OB for a punch travel of 40 mm. Numerical results obtained with the BST element are compared with those reported in NUMISHEET'93 conference (1993)

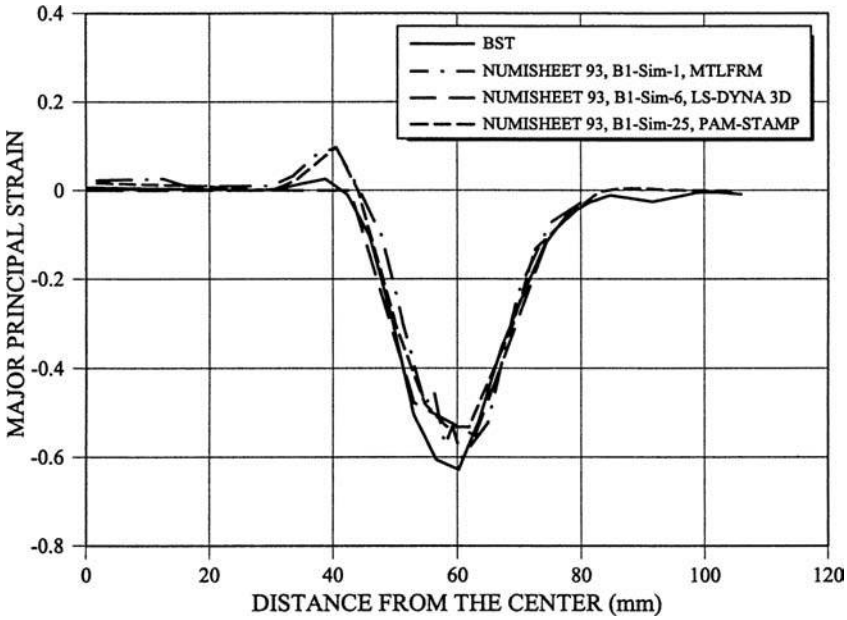

Figure 33.
Deep drawing of a square box. Distribution of major principal strain ε_2 along the line OB for a punch travel of 40 mm. Numerical results obtained with the BST element are compared with those reported in NUMISHEET'93 conference (1993)

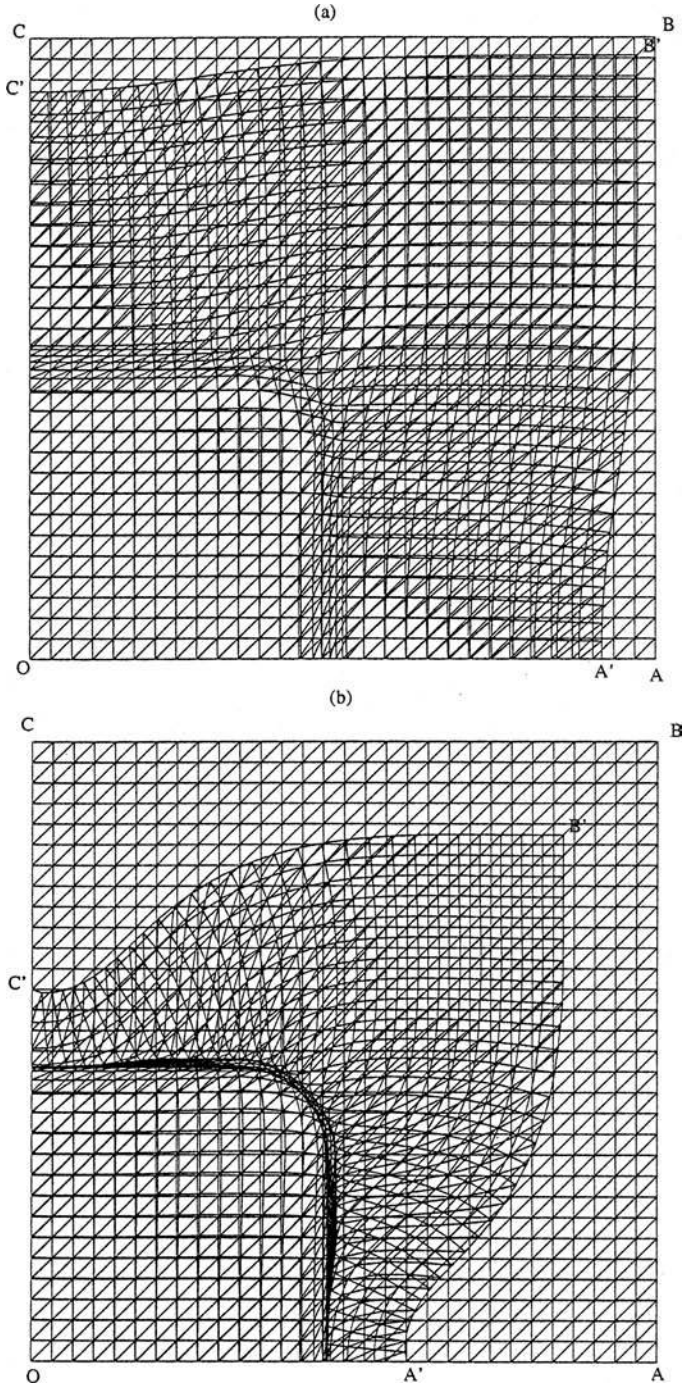

Figure 34.
Deep drawing of a square box. View of original and final sheet geometries for a punch travel of 40 mm

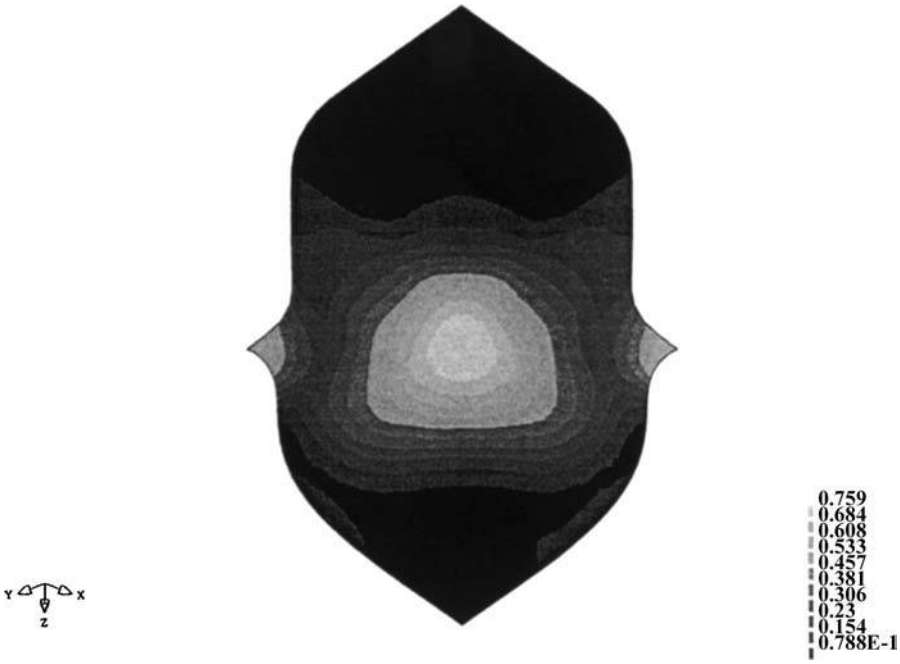

Figure 35.
Deep drawing of a square box. Distribution of effective plastic strain plotted over the deformed sheet geometry for a punch travel of 40 mm

discretizing the original flat sheet surface. The distribution of the actual/initial thickness ratio (h/h_0) over the deformed sheet surface (for a punch travel $H = 37$ mm.) is plotted in Figure 38. Further details of the analysis of this problem with the BST element are reported by Jovicevic and Oñate (1999).

6. Concluding remarks

The rotation-free BST element has proven to have an excellent performance in the explicit dynamic analysis of shells. Very good results have been obtained with relatively coarse meshes for a variety of non-linear shell dynamic problems involving frictional contact conditions.

The BST element is an excellent candidate for solution of practical engineering shell problems involving complex geometry, dynamics, material non-linearity and frictional contact conditions. Recent successful industrial applications of the BST element for practical sheet forming problems and crash-worthiness situations, among others, are reported by Jovicevic and Oñate (1999); Rojek *et al.* (1998); Oñate (1998) and Rojek and Oñate (1998).

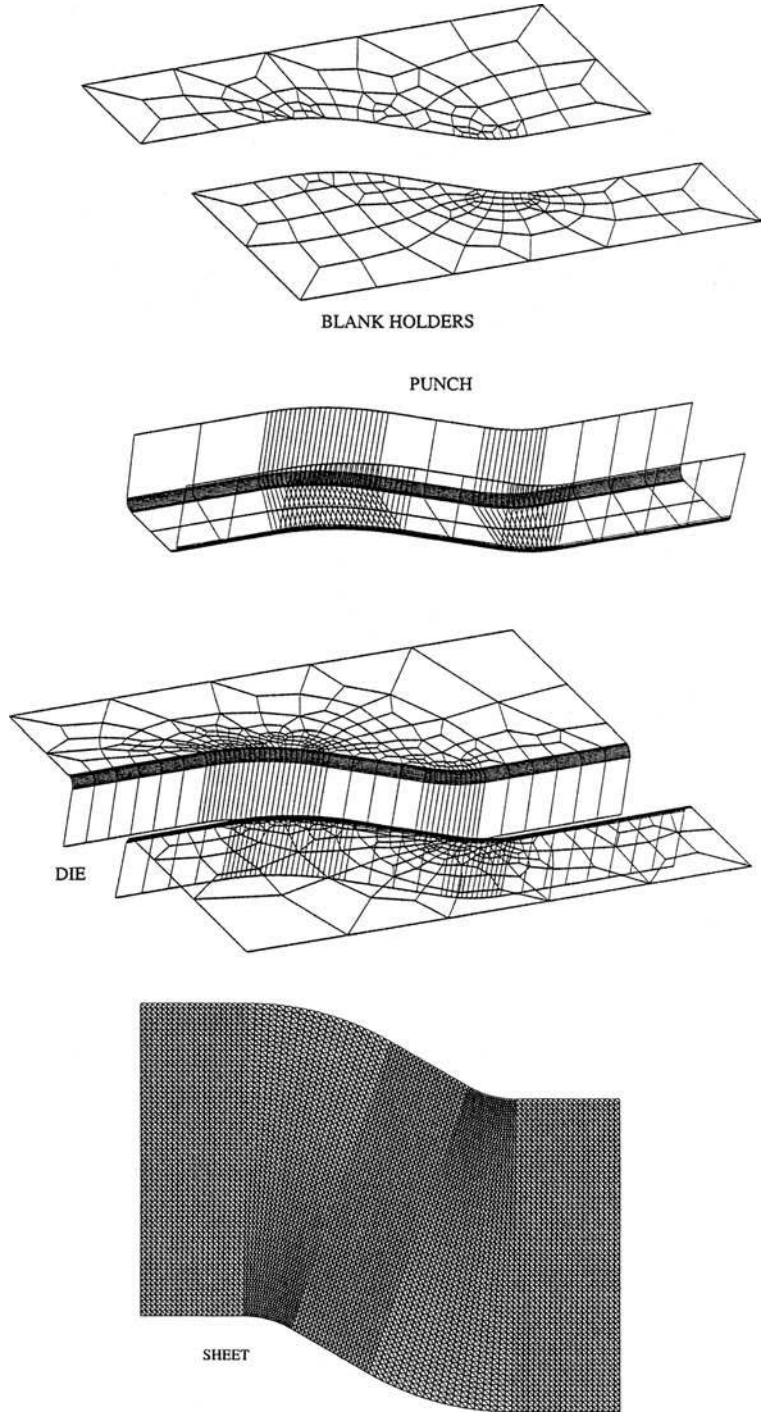

Figure 36.
Deep drawing of a curved rail. Discretization of the sheet into 1200 BST elements. The different tools are discretized using rigid triangles as shown in the figure

Young's modulus	69 Gpa
Poisson coefficient	0.3
Density	2730 kg/m^3
1D stress–strain law	$\bar{\sigma} = 589(10^{-4} + \bar{\varepsilon}_p)^{0.216}$
Radius of sheet	59.18 mm
Sheet thickness	1.0 mm
Punch radius	50.8 mm
Die radius	6.35 mm
Punch speed	10 s in (500 t) mm/s
Time of analysis	6.28 ms
Coulomb frictions coefficient	0.0 and 0.30

Table V.
Deep drawing of a square box. Material properties of mild steel

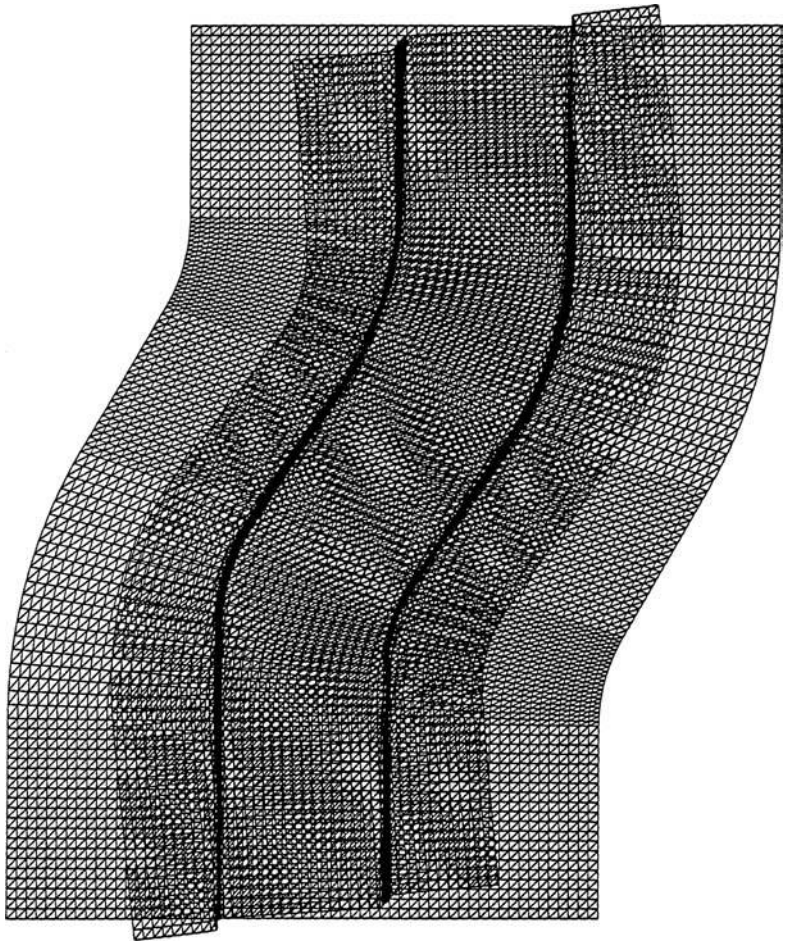

Figure 37.
Deep drawing of a curved rail. Deformed shape of the sheet mesh for a punch travel of 37 mm supersed to the original flat mesh

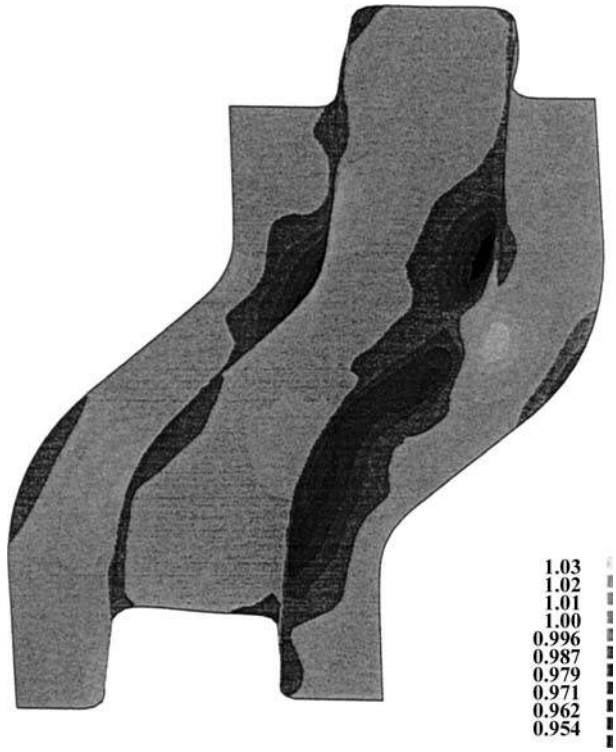

Figure 38.
Deep drawing of a curved rail. Distribution of thickness ratio values (h/h_0) plotted on the deformed sheet surface for a punch travel of 37 mm

References

Agelet de Saracibar, C. and Oñate, E. (1991), "Finite element analysis of sheet metal stamping processes" (in Spanish), Monograph M8, CIMNE, Barcelona.

Balmer, H.A. and Witmer, E.A. (1964), "Theoretical experimental correlation of large dynamic and permanent deformation of impulsive loaded simple structures", Air Force Flight Dynamic Lab., Rep. FDQ-TDR-64-108, Wright-Patterson, AFB, Ohio.

Bathe, K.J., Ramm, E. and Wilson, E.L. (1975), "Finite element formulation for large deformation dynamic analysis", *Int. J. Num. Meth. Eng.*, Vol. 9, pp. 353-86.

Batoz, J.L., Bathe, K.J. and Ho, L.W. (1980), "A study of three node triangular plate bending elements", *Int. J. Num. Meth. Eng.*, Vol. 15, pp. 1771-812.

Brunet, M. and Sabourin, F. (1994), "Prediction of necking and wrinkles with a simplified shell element in sheet forming", in Kröplin, B., (Ed.) *Int. Conf. of Metal Forming Simulation in Industry*, Vol. II pp. 27-48.

Bushnell, D. and Almroth, B.O. (1971), "Finite difference energy method for non linear shell analysis", *J. Computers and Structures*, Vol. 1, p. 361.

Cendoya, P., Oñate, E. and Miquel, J. (1997), "New finite elements for the elastoplastic dynamic analysis of shell structures" (In Spanish), Monograph M36, CIMNE, Barcelona.

Cirak, F., Ortiz, M. and Schröder, P. (2000), "Subdivision surfaces: a new paradigm for thin shell finite element analysis", *Int. J. Num. Meth. Eng.*, Vol. 47, pp. 2039-72.

Crisfield, M. (1997), *Non Linear Finite Analysis of Solids and Structures, Advanced topics*, J. Wiley Vol. 2.

Dienes, J.K. (1979), "On the analysis of rotation and stress rate in deforming bodies", *Acta Mechanica*, Vol. 32, pp. 217-332.

ECCOMAS (2000), Oñate *et al.* (Eds) *Proceedings of European Congress on Computational Methods in Applied Sciences and Engineering*. www.cimne.upc.es/eccomas.

Flores, F. and Oñate, E. (2001), "A basic thin shell triangle with only translational dofs for large strain plasticity", *Int. J. Num. Meth. Eng.*, Vol. 51, pp. 57-83.

Garcúa, C. "A numerical model for analysis of elastoplastic solids under large strains", PhD thesis, Universidad Politécnica de Cataluña, Barcelona.

Ghali, A. and Bathe, K.J. (1970), "Analysis of plates in bending using large finite elements", *Int. Association for Bridge and Structural Engineering Bulletin*, Vol. 30 No. II, pp. 29-40.

Hampshire, J.K., Topping, B.H.V. and Chan, H.C. (1992), "Three node triangular elements with one degree of freedom per node", *Eng. Comput.*, Vol. 9, pp. 49-62.

Hill, R. (1948), *A Theory of the Yielding and Plastic Flow of Anisotropic Metals*, Proc. Royal Soc., London, Volume A193 281 pp.

Idelsohn, S. and Oñate, E. (1994), "Finite volumes and finite elements: two 'good friends'", *Int. Journal Num. Meth. Eng.*, Vol. 37, pp. 3323-41.

Jovicevic, J. and Oñate, E. (1999), *Analysis of Beams and Shells Using a Rotation-free Finite Element-finite Volume Formulation*, Monograph 43, CIMNE, Barcelona.

Lee J.K., Wagoner R. and Nakamachi E. (1998), "A benchmark test for sheet metal forming analysis", Technical Report, Ohio State University.

Nay, R.A. and Utku, S. (1972), "An alternative to the finite element method", *Variational Methods Eng.*, Vol. 1.

Makinouchi, A., Nakamachi, E., Oñate, E. and Wagoner, R.H. (1993), "Numerical Simulation of 3-D Sheet Metal Forming Processes. Verification of Simulation with Experiment", *NUMISHEET'93, 2nd International Conference*: Isehara, Japan, 31 August-2 September.

NUMISHEET'96, 3rd International Conference: (1996), "Numerical simulation of 3-D sheet metal forming processes", Dearborn, Michigan, USA, 29 September-3 October.

Oñate, E. (1998), "Derivation of stabilized equations for numerical solution of advective-diffusive transport and fluid flow problems", *Int. J. Num. Meth. Eng.*, Vol. 151, pp. 233-65.

Oñate, E. (1999), "A review of some finite element families for thick and thin plate and shell analysis", in Hughes, T.J.R., Oñate, E., Zienkiewicz, O.C., (Eds) *Recent development in finite element analysis*, CIMNE, Barcelona.

Oñate, E. and Agelet de Saracibar, C. (1991), "Finite element analysis of sheet metal forming problems using a selective voided viscous shell membrane formulation", *Int. Journal for Numerical Methods in Engineering*, Vol. 30, pp. 1577-93.

Oñate, E. and Cervera, M. (1993), "Derivation of thin plate bending elements with one degree of freedom per node", *Eng. Comput.*, Vol. 10, pp. 543-61.

Oñate, E. and Zárate, F. (2000), "Rotation free triangular plate and shell elements", *Int. J. Num. Meth. Eng.*, Vol. 47, pp. 557-603.

Oñate, E., Cervera, M. and Zienkiewicz, O.C. (1994), "A finite volume format for structural mechanics", *Int. J. Num. Meth. Eng.*, Vol. 37, pp. 181-201.

Phaal, R. and Calladine, C.R. (1992a), "A simple class of finite elements for plate and shell problems. I: Elements for beams and thin plates", *Int. J. Num. Meth. Eng.*, Vol. 35, pp. 955-77.

Phaal, R. and Calladine, C.R. (1992b), "A simple class of finite elements for plate and shell problems. II: An element for thin shells with only translational degrees of freedom", *Int. J. Num. Meth. Eng.*, Vol. 35, pp. 979-96.

Rio, G., Tathi, B. and Laurent, H. (1994), "A new efficient finite element model of shell with only three degrees of freedom per node. Applications to industrial deep drawing test", in Barata Marques, M.J.M., (Ed.) *Recent Developments in Sheet Metal Forming Technoloy*, 18th IDDRG Biennial Congress, Lisbon.

Rojek, J. and Oñate, E. (1998), "Sheet springback analysis using a simple shell triangle with translational degrees of freedom only", *Int. J. of Forming Processes*, Vol. 1 No. 3, pp. 275-96.

Rojek, J., Oñate, E. and Postek, E. (1998), "Application of explicit FE codes to simulation of sheet and bulk forming processes", *J. of Materials Processing Technology*, Vol. 80-81, pp. 620-7.

Simo, J.C., Fox, D.D. and Rifai, M.S. (1990), "On stress resultant geometrically exact shell model. Part III: Computational aspects of the nonlinear theory", *Comput. Meth. Appl. Mech. Eng.*, Vol. 79, pp. 21-70.

STAMPACK. (2002), *A finite element system for analysis of sheet stamping processes*. Quantech ATZ SA. www.quantech.es.

Stolarski, H., Belytschko, T. and Carpenter, N. (1984), "A simple triangular curved shell element", *Eng. Comput.*, Vol. 1, pp. 210-8.

Stolarski, H., Belytschko, T. and Lee, S.-H. (1995), "A review of shell finite elements and corotational theories", *Computational Mechanics Advances*, Vol. 2 No. 2 North-Holland.

Timoshenko, S.P. (1979), *Theory of Plates and Shells*, McGraw Hil, New York.

Uguraz, A.C. (1981), *Stresses in Plates and Shells*, McGraw Hill, New York.

WHAMS-3D, "An explicit 3D finite element program", KBS2 Inc., Willow Springs, Illinois 60480, USA.

Yang, D.Y., Jung, D.W., Song, L.S., Yoo, D.J. and Lee, J.H. (1993), "Comparative investigation into implicit, explicit and iterative implic/explicit schemes for simulation of sheet metal forming processes", in Makinouchi, A., Nakamachi, E., Oñate, E., Wagoner, R.H. (Eds) *NUMISHEET'93*, RIKEN, Tokyo pp. 35-42.

Zhong, Z.H. (1993), *Finite Element Procedures for Contact Impact Problems*, Oxford University Press, Oxford, UK.

Zienkiewicz, O.C. and Oñate, E. (1991), "Finite elements versus finite volumes. Is there really a choice?", in Wriggers, P., Wagner, W., (Eds) *Nonlinear Computation Mechanics. State of the Art*, Springer Verlag, Berlin.

Zienkiewicz, O.C. and Taylor, R.C. (2000), *The Finite Element Method*, 5th ed., Butterworth-Heinemann Vol. 2.

This article has been cited by:

1. Jiabei Shi, Zhuyong Liu, Jiazhen Hong. 2018. Dynamic contact model of shell for multibody system applications. *Multibody System Dynamics* **44**:4, 335-366. [Crossref]
2. G. Wang, X. Y. Cui, G. Y. Li. 2016. A rotation-free shell formulation using nodal integration for static and dynamic analyses of structures. *International Journal for Numerical Methods in Engineering* **105**:7, 532-560. [Crossref]
3. Stian F. Johnsen, Zeike A. Taylor, Matthew J. Clarkson, John Hipwell, Marc Modat, Bjoern Eiben, Lianghao Han, Yipeng Hu, Thomy Mertzanidou, David J. Hawkes, Sebastien Ourselin. 2015. NiftySim: A GPU-based nonlinear finite element package for simulation of soft tissue biomechanics. *International Journal of Computer Assisted Radiology and Surgery* **10**:7, 1077-1095. [Crossref]
4. Dalia Calneryte, Rimantas Barauskas. Dynamic Analysis of 4-Node Degenerated Shell Element with Updated Thickness 592-603. [Crossref]
5. Y.X. Zhou, K.Y. Sze. 2012. A geometric nonlinear rotation-free triangle and its application to drape simulation. *International Journal for Numerical Methods in Engineering* **89**:4, 509-536. [Crossref]
6. Gang Zheng, Xiangyang Cui, Guangyao Li, Suzhen Wu. 2011. An edge-based smoothed triangle element for non-linear explicit dynamic analysis of shells. *Computational Mechanics* **48**:1, 65-80. [Crossref]
7. Eugenio Oñate, Francisco Zárate. 2010. Extended rotation-free plate and beam elements with shear deformation effects. *International Journal for Numerical Methods in Engineering* n/a-n/a. [Crossref]
8. J. G. Valdés, E. Oñate. 2009. Orthotropic rotation-free basic thin shell triangle. *Computational Mechanics* **44**:3, 363-375. [Crossref]
9. Fernando G. Flores, Carlos F. Estrada. 2007. A rotation-free thin shell quadrilateral. *Computer Methods in Applied Mechanics and Engineering* **196**:25-28, 2631-2646. [Crossref]
10. Fernando G. Flores, Eugenio Oñate. 2007. A rotation-free shell triangle for the analysis of kinked and branching shells. *International Journal for Numerical Methods in Engineering* **69**:7, 1521-1551. [Crossref]
11. Fernando G. Flores, Eugenio Oñate. 2006. Rotation-free finite element for the non-linear analysis of beams and axisymmetric shells. *Computer Methods in Applied Mechanics and Engineering* **195**:41-43, 5297-5315. [Crossref]
12. Eugenio Oñate, Fernando G. Flores. 2005. Advances in the formulation of the rotation-free basic shell triangle. *Computer Methods in Applied Mechanics and Engineering* **194**:21-24, 2406-2443. [Crossref]
13. John Argyris, Manolis Papadrakakis, Zacharias S. Mouroutis. 2003. Nonlinear dynamic analysis of shells with the triangular element TRIC. *Computer Methods in Applied Mechanics and Engineering* **192**:26-27, 3005-3038. [Crossref]